International Journal of Solids and Structures 312 (2025) 113260

Contents lists available at ScienceDirect

International Journal of Solids and Structures

journal homepage: www.elsevier.com/locate/ijsolstr

# A directional contraction method to model sand-based binder jet 3D printed materials

Elodie Donval [a], Matti Schneider [a,b,*], Hannes Grimm-Strele [b], Michael Godehardt [b], Raphael Burger [c], Philipp Lechner [d], Daniel Günther [c], Heiko Andrä [b]

[a] Institute of Engineering Mathematics, University of Duisburg–Essen, Germany
[b] Fraunhofer Institute for Industrial Mathematics ITWM, Kaiserslautern, Germany
[c] Fraunhofer Institute for Casting, Composite and Processing Technology IGCV, Garching, Germany
[d] Institute of Materials Resource Management, University of Augsburg, Germany

ARTICLE INFO

*Keywords:*
Sand binder jetting
Microstructure generation
Stacked mechanical contraction method
FFT-based computational micromechanics
Porous media
Sand core

ABSTRACT

The development of binder-jet sand-based 3D printing allows a quick design of complex parts for foundry molds. To ensure a good quality of casting, the mold must feature some specific mechanical, thermal and transport properties. In that context, a reliable modeling approach for the sand-core material provides a less expensive alternative to extended experimental campaigns. In the present paper, we propose a physics-based microstructure generation approach that is able to capture the experimentally observed anisotropy of the sand-binder composite. The corresponding packing algorithm features a directional contraction of the unit cell that mimics the layer-by-layer deposition of the sand. We also introduce an improved, grid-free approach to add binder between the grains. After the microstructure generation process, we compute the apparent stiffness and permeability on the generated microstructure, and show that these apparent properties are transversely isotropic in the vertical direction. We provide a parametric study on some parameters of interest, such as the volume fraction of binder or the layer thickness. Finally, the results obtained through our modeling approach are compared to experimental results available in the literature. These comparisons show that the anisotropy induced by our microstructure generation approach is similar to the one experimentally observed.

## 1. Introduction

Sand binder jetting of cores for the foundry allows designing more complex shapes than the conventional core shooting process and printing directly from a CAD model (Upadhyay et al., 2017; Sivarupan et al., 2021). In addition, sand-based binder jetting 3D printing of sand materials has several applications in research, e.g., to create model rocks (Zhou and Zhu, 2018; Braun et al., 2021; Zhao et al., 2023), and to study the behavior of masonry at a reduced scale (DeJong and Vibert, 2012; Del Giudice and Vassiliou, 2020). These industrial and academic applications have fostered the need for a better understanding of the 3D printing process and its relationship to the properties of the produced composite material.

Sand binder jetting features a layer-by-layer grains deposition process as well as a selective addition of binder (Upadhyay et al., 2017). More specifically, a layer of sand, typically between 280 μm and 500 μm thick (Sivarupan et al., 2021), is first deposited into a job box using a recoater. A print head then selectively adds binder to the areas that make up the part to be printed. Once the entire layer is printed, the job box moves down a distance equal to the layer thickness and the process is repeated. After the part is fully printed, the binder must cure for several hours or days, depending on the curing conditions, to reach its final mechanical properties (Mitra et al., 2018). The latter process may be accelerated by a heat treatment (Mitra et al., 2019).

In the context of casting, the thermo-poro-mechanical properties of the sand core directly influence the geometric and mechanical properties of the cast object. As the sand binder jetting process is different from conventional core blowing, research had to be undertaken to understand the influence of this novel process on the properties of the printed sand core. Relying on CT scanning, Kong et al. (2019) showed that the layer-by-layer printing process leads to an anisotropic arrangement of the grains within the microstructure. Mitra et al. (2020) investigated the formation of the binder bridges, while Dana and El Mansori (2020) provided insights into the failure mechanism of the composite, which occurs mainly at the binder bridges. Anisotropic transport properties were highlighted by Coniglio et al. (2018) and Sivarupan et al. (2019). Del Giudice et al. (2024) studied the effect

* Corresponding author at: Institute of Engineering Mathematics, University of Duisburg–Essen, Germany.
*E-mail address:* matti.schneider@uni-due.de (M. Schneider).

https://doi.org/10.1016/j.ijsolstr.2025.113260
Received 21 November 2024; Received in revised form 29 January 2025; Accepted 31 January 2025
Available online 12 February 2025

of the binder content on the anisotropic elastic properties. Several authors, including Zhang et al. (2023) and Seshadri et al. (2021), also showed that the strength properties are anisotropic. However, all the cited studies are experimental and focus on a specific choice of sand and binder. In particular, most studies focus on 3D printing with organic binders, which are known to be carcinogenic (Upadhyay et al., 2017) and tend to be replaced by inorganic binders for casting applications. Moreover, the previously cited studies focus predominantly on the macroscopic behavior of the 3D printed composite, and do not allow for a complete understanding of the phenomena causing the anisotropy. In this context, a multiscale modeling tool would provide insights on the influence of the printing parameters on the properties of the 3D printed material. The existing numerical studies of the 3D printing process mostly focus on the surface aspect of the mold as well as its local density, and are based on DEM simulations. For instance, Zhang et al. (2022) and Weissbach et al. (2024) studied the roller spreading strategies and their influence on the local particles density.

As it can be observed on CT-scans (Kong et al., 2019), the material obtained through sand binder jetting is porous and comprises grains bonded by a low volume fraction of binder. Such a microstructure presents similarities with the microstructure of lightly cemented granular materials (Mavko et al., 2020). For isotropic cemented materials, Dvorkin et al. (1994, 1999) pioneered analytical approaches based on the average coordination number to determine the effective elastic properties of cemented granular materials. The coordination number of a particle is defined by the number of other particles which are bonded to it, and does not provide any information on the spatial repartition of the bonded particles or on their orientation. Therefore, the sole knowledge of the coordination number is not sufficient to describe an anisotropic structure. A first alternative to Dvorkin et al.'s analytical approaches is to generate the microstructure through the distinct element method (Cundall and Strack, 1979). Then, the mechanical properties of the sand-binder assembly are computed using the distinct element method (Theocharis et al., 2020; Shen et al., 2022) or through lattice methods (Topin et al., 2007; Sattari et al., 2017). Another option is to resort to image-based computations, either relying on CT scans (Andrä et al., 2013a,b) or on computer generated microstructures (Bargmann et al., 2018). As an example, Lienhard et al. (2024) computed the mechanical properties of 3D printed and injection molded fiber-reinforced composites based on CT scans. Returning to the original sand core topic, Schneider et al. (2018) and Ettemeyer et al. (2020) determined the thermal, transport, and mechanical properties of a shot sand core material based on computer generated microstructures. However, the core shooting process produces a material which is isotropic on average, and so does the related microstructure generation approach. Therefore, it is imperative to develop a microstructure generation technique which reflects the inherent anisotropy of the manufacturing process.

In the present paper, we aim to understand the influence of the process parameters on the macroscopic behavior of the 3D printed material. More precisely, we focus on the relationship between the geometry of the 3D printed composite's microstructure, the properties of its components, and its macroscopic behavior. The main contribution of the article at hand are:

1. a microstructure model for a 3D printed sand core,
2. 3D image based computations which shed light on the microstructure-properties relationship for the material at hand,
3. and a validation of the approach with respect to experimental results available in the literature.

Of key importance here is an approach to *generate* the microstructures in a flexible, robust and accurate way. To do so, we use the methodology proposed by Schneider et al. (2018) as a starting point. First, the sand grains' shape is obtained by a $\mu$CT scan and approximated by a set of spheres. Then, the grains are packed to the desired volume fraction. Finally, binder is added between the grains. The choices made for each of these three modeling steps are justified in the next paragraphs. The initial approach (Schneider et al., 2018) is however not sufficient to account for several aspects of the 3D printing process. Indeed, the sand deposition tends to give a preferred orientation to the grains. Moreover, the 3D printing process is sequential, and the position of the particles of an existing layer should be little influenced by the addition of a new layer. The packing algorithm proposed in the present paper extends Schneider et al.'s methodology to account for these specificities. We also propose several improvements to the aforementioned approach to decrease its algorithmic complexity and to increase the accuracy of the geometrical description of the sand-binder composite.

Several approaches are found in the literature to describe particles, see the comprehensive review (Bargmann et al., 2018). Spheres and ellipsoids are the most simple ones, however they are often too simple to capture the features conducing to the complex behavior and interactions of a set of particles (Lu et al., 2015). Some more complex shapes such as superquadric (Preece et al., 1999; Soltanbeigi et al., 2018), polyhedra (Hosseininia and Mirghasemi, 2006; Lu et al., 2017) or NURBS-based shapes (Andrade et al., 2012) capture the grain shape more accurately, however contact detection is more complex to handle, especially for non-convex particles. Clusters of spheres (Katagiri et al., 2010; Ferellec and McDowell, 2010), also known as clumps (Angelidakis et al., 2021), present both the ability to describe the shape of the grain accurately and the advantage of a rather simple contact detection. Their main drawbacks, namely their inability to account for sharp edges and to provide accurate surface data for friction, have a rather low impact in the present case. Indeed, the mechanical behavior of the sand-binder composite is mainly driven by binder bridges between particles rather than by direct particle-to-particle contacts.

The choice of the packing algorithm is closely linked to the particle approximation. We wish to pack the grains to a rather high volume fraction, usually between 44% and 50% (Coniglio et al., 2018) for a composite obtained by sand binder jetting. Such volume fractions lie outside of the applicability range of the celebrated RSA (Feder, 1980) (Random Sequential Adsorption) approach. When it comes to spheres, algorithms were developed to reach high volume fractions, such as level-set assisted RSA (Sonon et al., 2012), sedimentation methods (Bennett, 1972; Pilotti, 1998), approaches based on linear programming methods (Torquato and Jiao, 2010), for instance. Several algorithms, in particular based on molecular dynamics (Lubachevsky and Stillinger, 1990), include physics-based behaviors. Among those algorithms, the Mechanical Contraction Method (MCM) proposed by Williams and Philipse (2003) was extended by Schneider et al. (2018) to clusters of overlapping spheres. We introduce an extension of the MCM which accounts for the layer-by-layer deposition of the grain by performing the contraction operation in the vertical direction only. This process tends to give the grains a preferred orientation similar to the one they acquire because of gravity. Approaches relying on a layer-by-layer deposition model and realistic particles were proposed for other additive manufacturing techniques, such as the cold-spray process (Delloro et al., 2017). One main difference between binder jetting and cold spray is the density of particles added. Indeed, in the cold spray process, the added particles may be considered individually without interactions with other moving particles, while moving particles interact with each other in the binder jetting process. Returning to the stacked mechanical contraction method, soft box boundary constraints are added in the stacking direction to force the grains to remain in their original layer. The proposed approach account for the sequential generation of several layers of sand in order to reproduce the 3D printing process. Once one layer is generated and the target volume fraction is reached, the position of the grains composing that layer is frozen. An additional layer is then generated on top of this initial one, following the same vertical contraction process. Through several examples, we demonstrate that the proposed approach is able to generate anisotropic microstructures. We also show that the anisotropy of the generated microstructures is of a similar order as observed experimentally through existing studies in the literature.

Once the grains are packed to the desired volume fraction, the binder phase is added. In Schneider et al. (2018), the binder addition step was performed through mathematical morphology operations, namely a closing operation. This approach is quantitized and depends on the discretization grid. In the following, we propose a level-set (Osher and Sethian, 1988) based description of the binder. Such an approach relies on the outer signed distance function of clusters of overlapping spheres. Indeed, it is possible to exhibit a simple analytical expression of the outer signed distance of the union of spheres, which is actually the distance to the closest sphere. The boundary of the cluster is defined as a level-set of zero. We introduce a smoothed boundary of the cluster based on a smoothed version of this zero-level set, and we propose to define the domain occupied by the binder as the domain comprised between the smoothed boundary and the boundary of the cluster.

The outline of the paper is the following. The details of the microstructure generation approach are presented in Section 2. Then, we assess the anisotropy of the microstructure through computational homogenization of its effective elastic properties and transport properties. These two properties are of particular interest with regards to sand cores because they directly influence the surface quality and the mechanical properties of the casted part. In Section 3, we introduce the FFT-based homogenization framework (Moulinec and Suquet, 1994, 1998) for the elastic properties as well as the permeability homogenization framework, relying on Stokes' equations. We perform several studies to determine the ideal resolution and size of the unit cell to get the effective properties of the sand-binder composite. Finally, in Section 4, we propose several applicative examples. First, we perform parametric studies on two printing parameters of interest, namely the layer thickness and the binder content, and on the sand and binder elastic properties. Then, we compare our numerical results to experiments conducted on the elastic behavior of the composite obtained through sand binder jetting by Del Giudice et al. (2024), and on its transport properties by Coniglio et al. (2018).

## 2. Presentation of the microstructure generation approach

### 2.1. Approximation of the sand grains as clusters of overlapping spheres

The approximation of the particles by clusters of spheres (Ferellec and McDowell, 2010; Li et al., 2015; Angelidakis et al., 2021) leads to realistic particles, while preserving the advantageous contact detection properties of spherical particles. Garcia and coworkers (Garcia et al., 2009; Garcia, 2009) proposed an algorithm in order to approximate any convex or non-convex particle as a cluster of overlapping spheres. This algorithm was improved by several authors (Li et al., 2015; Yuan, 2019) and implemented in the context of inorganically-bound shot sand cores by Schneider et al. (2018).

As a first step, a 3D image of each sand grain is needed. To extract such an image, a $\mu$CT scan with a 4 µm resolution was conducted on a GS14 sand sample without binder. The grains were separated by the classical morphological approach based on the watershed transform applied to the inverted Euclidean distance image. The inevitable oversegmentation is usually prevented by smoothing the inverted distance image by the h-minima (also called h-dome) transform or by preflooding the watershed transform. It is possible to adapt the parameter of the h-minima transform to the gray values such that even sand grains with complex shape are separated almost perfectly (Burgmann et al., 2022). However, such a strategy is harder to parametrize. Here, we follow a more robust variant. Preflooding is followed by removing watersheds that are large compared to the grain fragments they separate, as described in Ettemeyer et al. (2020). The volume threshold for preflooding is chosen rather small in magnitude to ensure that no undersegmentation occurs, whereas the area threshold for the watersheds is found heuristically. This strategy leaves only a few oversegmented grains to be corrected interactively in the end. Taking this idea further, Alshembar et al. (2024) trained random forests operating on geometric features of the two fragments and their dividing watershed to correct the oversegmentation fully automatically. In total, 15 960 grains were identified for that scan, see Fig. 1(a) for a slice. The grains intersecting the bottom or the top layer of the sample were considered incomplete and thus not considered. Fig. 1(b) shows one of the extracted grains.

As second step, we identify the cluster of overlapping spheres approximation of a grain from its 3D image. A cluster with index $i$ of $n_i$ overlapping spheres is defined as the following set of points $\boldsymbol{x}$:

$$\left\{\boldsymbol{x} \in \mathbb{R}^3 \text{ such that } \|\boldsymbol{x} - \boldsymbol{c}_i - \boldsymbol{v}_{ia}\| \leq r_{ia} \text{ for at least one } a \in \{1, 2, \dots, n_i\}\right\} \tag{2.1}$$

In Eq. (2.1), $\boldsymbol{c}_i \in \mathbb{R}^3$ denotes the position of the cluster's centroid, $\boldsymbol{v}_{ia} \in \mathbb{R}^3$ refers to the position of the $a$th sphere relatively to the cluster's centroid, and $r_{ia} \in \mathbb{R}^+$ stands for the radius of the $a$th sphere. Therefore, we seek an algorithm to cover a given fraction $\alpha$ of the volume of the 3D image of the grain with the smallest possible number of spheres. An approximate solution to this so-called "set cover problem" can be achieved in a polynomial time by a greedy algorithm. The initial approach introduced by Garcia et al. (2009) and Garcia (2009) is summed up in algorithm 1.

**Algorithm 1** Garcia's (Garcia et al., 2009; Garcia, 2009) cluster of overlapping spheres algorithm

```
Identify all potential spheres
Add largest sphere to cluster
while V_cluster < α V_particle do
    Choose sphere with largest potential coverage and connected to the current cluster
    Add sphere to cluster
end while
```

In algorithm 1, the potential coverage of a sphere corresponds to the volume that would be added to the existing cluster if the considered sphere was added. The target coverage threshold $\alpha$ corresponds to the percentage of the grain volume which is covered by the cluster of overlapping spheres. Fig. 1(c) shows a grain's approximation by a cluster of overlapping spheres for several values of target coverage $\alpha$. In Fig. 1(c), the resolution for the clusters of overlapping spheres is chosen identical to the one of the initial image. In the following, we use a coverage value $\alpha = 90\%$, leading to around 150–200 spheres per cluster. This value of $\alpha$ is identical to the one used in Schneider et al. (2018). According to Garcia et al. (2009), at least 100 spheres are necessary to correctly approximate the inertia tensor of the particle.

The naive implementation of Garcia's (Garcia et al., 2009; Garcia, 2009) approach has a complexity of $O(N^6)$. However, this complexity is reduced to $O(N^3 \log N)$ using the following tricks.

1. **Identifying all potential spheres**: Garcia's approach considers the center of each voxel composing the particle in the initial 3D image as a center of a potential sphere. To determine the radius of the largest sphere contained in the grain, the radius of a candidate sphere is increased step-by-step by the length of a voxel edge until the sphere hits the boundary of the particle. The complexity of this step can be decreased from $O(N^6)$ to $O(N^3 \log N)$ by determining the distance from each voxel center within the initial particle to the boundary by a fast-marching approach (Sethian, 1999), which is closely related to computing the Euclidean distance transform (Danielsson, 1980; Borgefors, 1984).
2. **Approximated 3D thinning of the structure**: Not all the spheres identified in step **1** need to be considered to reconstruct the initial particle. Actually, the particle may be fully reconstructed by considering only the spheres whose center lies on the medial surface (Blum, 1967) of the particle. The medial

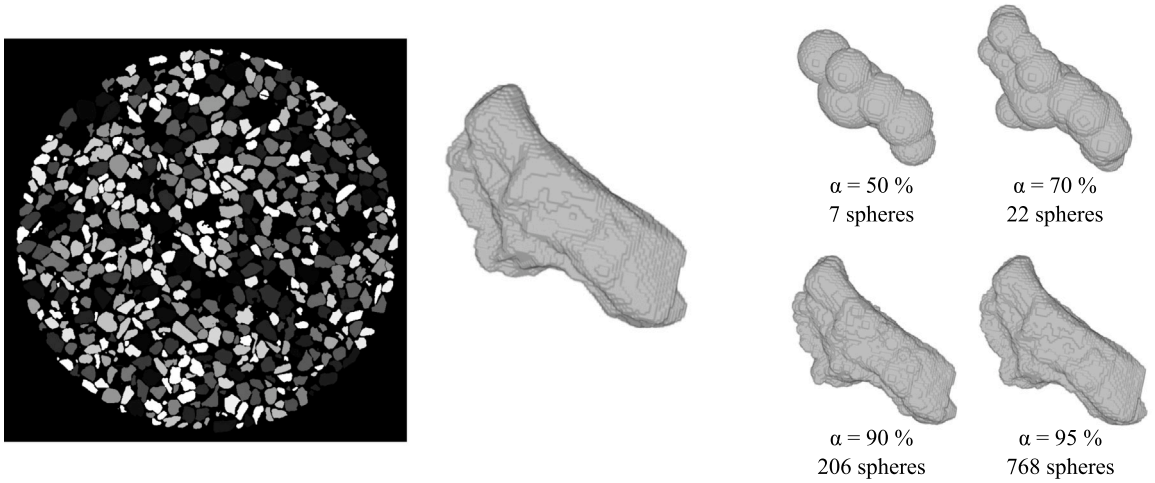


(a) Slice of the original $\mu$CT scan (b) One grain extracted from the CT scan (c) CoS approximation of the grain represented in figure 1(b)

**Fig. 1.** Cluster of overlapping spheres approximation process.

surface consists of all the points of the particle which are the center of a maximal inscribed sphere touching at least two points of the boundary of the particle. The medial surface may be approximated by a thinning of the particle (Beucher, 1994). Yuan's (2019) approach relies on this idea and improves the approach initially proposed by Garcia by only considering spheres whose center belongs to the skeleton obtained by thinning. We use a similar approach, and chose to approximate the medial surface relying on the signed distance function to the particle boundary which was computed in item **1**. If a point is a saddle point on the signed distance function map, then it is assumed to be part of the medial surface. Because this approach allows to consider a reduced amount of spheres as potential candidates, the computation time is also reduced. In our experience, a speed-up by a factor three can be expected.

3. **Choosing the sphere with the largest coverage**: Garcia's approach iterates on the spheres, ordered by decreasing radius, to find the sphere with the largest potential coverage. Hence, the potential coverage of a large number of spheres needs to be updated every time a sphere is added to the cluster. This operation is extremely time-consuming, and can be drastically sped-up by choosing the proper kind of data structure. In our implementation, spheres are ordered by potential coverage in a min-heap structure (Williams, 1964). To choose the sphere to add to the cluster, the potential coverage of the sphere which had the maximal potential coverage at the beginning of the previous step is updated, and the heap is updated. If the sphere with the maximal coverage changes, the procedure is repeated. In the opposite case, the considered sphere is chosen to integrate the cluster. This approach leads to significantly less updates of potential coverages, and hence, to a significant speed up of the computation, by a factor of 67.5 if we consider a square particle of side 100 voxels and a coverage threshold of $\alpha = 90\%$.

The computation time for the particles extracted from the CT scan and for a coverage value $\alpha = 90\%$ ranges from 0.1 to 3 s on a standard laptop with an Intel i5 CPU and 32 Gb of RAM. It should be noted that the approximation of the grains as clusters of overlapping spheres needs to be performed only once for a given value of coverage. After this approximation step, the cluster of overlapping spheres are stored as a particle library, from which particles are drawn during the grain packing step. For the study performed in this paper, all 15 960 grains were included in the particle library at first. However, the computations are performed on a reduced-size library of 200 particles. This choice enables a better homogeneity in the results presented in the paper. The 200 particles were chosen by a quasi-random Sobol sampling performed on the diameter of the bounding sphere of each grain, so that the grain size distribution of the reduced library is similar to the initial one. Finally, we note that all microstructures investigated in this study, except for the $(1120^2 \times 560)$ µm$^3$ ones presented in Fig. 6, comprise less than 200 grains.

### 2.2. Grain packing by a stacked mechanical contraction method

The mechanical contraction method (MCM) was initially proposed by Williams and Philipse (2003) to pack spheres and spherocylinders to high volume fractions, up to 63.1% for a monodisperse distribution of spheres. Its extension to clusters of overlapping spheres, proposed by Schneider et al. (2018), proved able to pack non-convex sand-grain particles to volume fractions up to 68 %. The principle of the original MCM is the following. Suppose that we wish to generate a microstructure occupying a volume $Y = [0, L_x] \times [0, L_y] \times [0, L_z]$ where $L_x$, $L_y$ and $L_z$ are the dimensions of the microstructure. This microstructure should comprise $N$ particles, described as clusters of overlapping spheres, in a volume fraction $\eta$. The first step is to randomly sampling the $N$ particles, in a larger volume $Y'$ defined by:

$$Y' = [0, \beta L_x] \times [0, \beta L_y] \times [0, \beta L_z], \text{ with a factor } \beta \gg 1. \tag{2.2}$$

As part of the sampling process, the particle, i.e., its description as a cluster of overlapping spheres, is sampled from the grain library generated in Section 2.1. The initial position of its centroid $\boldsymbol{c}_i \in \mathbb{R}^3$ and its initial orientation, as a rotation matrix $\boldsymbol{R}_i \in SO(3)$, are also sampled. In the initial configuration, the grains should not overlap, which is made easier by the low volume fraction of grains.

From the initial configuration, the MCM algorithm alternates between two phases: a contraction phase and an overlap removal phase. The contraction phase consists in reducing the size of the volume by reducing the coefficient $\beta$. The position of the grains' centroids $\boldsymbol{c}_i$ is scaled accordingly, but their size and orientation remains unchanged. After a contraction phase, some grains may overlap. The non-overlapping condition between two clusters $i$ and $j$ writes:

$$\begin{aligned} &\text{dist}_{Y'}(\boldsymbol{c}_i + \boldsymbol{R}_i \boldsymbol{v}_{ia}, \boldsymbol{c}_j + \boldsymbol{R}_j \boldsymbol{v}_{jb}) \geq r_{ia} + r_{jb} \\ &\quad \text{for all } 1 \leq i < j \leq N,\ a \in \{1, 2, \dots, n_i\},\ b \in \{1, 2, \dots, n_j\}, \end{aligned} \tag{2.3}$$

where $\mathrm{dist}_{Y'}$ refers to the periodic Euclidean distance with respect to the considered cell $Y'$. Introducing the quantity $\delta_{ij}$:

$$\delta_{ij} = \max\left(0, \max_{1\le a\le n_i, 1\le b\le n_j}\left[r_{ia} + r_{jb} - \mathrm{dist}_{Y'}(\boldsymbol{c}_i + \boldsymbol{R}_i\boldsymbol{v}_{ia}, \boldsymbol{c}_j + \boldsymbol{R}_j\boldsymbol{v}_{jb})\right]\right), \tag{2.4}$$

the non-overlapping condition defined in Eq. (2.3) can also be rewritten as an equality condition:

$$\delta_{ij} = 0 \quad \text{for all } 1 \le i < j \le N. \tag{2.5}$$

We define the overlapping energy $\mathcal{E}$ as:

$$\mathcal{E}(\boldsymbol{c}_1, \dots, \boldsymbol{c}_N, \boldsymbol{R}_1, \dots, \boldsymbol{R}_N) = \frac{1}{2}\sum_{1\le i<j\le N}\delta_{ij}^2. \tag{2.6}$$

Then, the non-overlapping condition (2.5) also writes:

$$\mathcal{E}(\boldsymbol{c}_1, \dots, \boldsymbol{c}_N, \boldsymbol{R}_1, \dots, \boldsymbol{R}_N) = 0. \tag{2.7}$$

Schneider et al. (2018) interpreted the approach proposed by Williams and Philipse (2003) as minimizing the overlapping energy $\mathcal{E}$ by a gradient descent to find a non-overlapping configuration. In the context of clusters of overlapping spheres, we consider the same formulae as Schneider et al. (2018) to update the position $\boldsymbol{c}_i$ and orientation $\boldsymbol{R}_i$ of the particles:

$$\boldsymbol{c}_i \leftarrow \boldsymbol{c}_i - h_c\nabla_{\boldsymbol{c}_i}\mathcal{E} \quad \text{and} \quad \boldsymbol{R}_i \leftarrow \text{-}\exp\left(h_R\nabla_{\boldsymbol{R}_i}\mathcal{E}\right)\boldsymbol{R}_i, \tag{2.8}$$

where exp denotes the matrix exponential, and $\nabla\mathcal{E}$ is the gradient of the overlapping energy. In the following, we consider the step-size values $h_c = 0.1$ and $h_R = 0.4$. The overlap-energy minimization and position update phase runs until the overlap energy reaches zero, or, in practice, the machine precision. Then, it is possible to move on to the next contraction phase until the target volume fraction is reached.

In the above-described packing approach, an identical contraction factor is applied in all three directions, resulting in microstructures which are close to being isotropic. Hence, despite its advantages, the classical MCM is not adapted to describe the anisotropic materials obtained through 3D printing. For this reason, we introduce an extension of the MCM which we refer as the "Stacked Mechanical Contraction Method" (stacked MCM). This variant takes into account the layer-by-layer deposition process induced by 3D printing. Let us assume that, during the 3D printing process, the layers are generated in the $(x, y)$-plane. The $z$-direction is referred as the stacking direction. The two main differences between the classical MCM and the stacked MCM are the following.

1. In the stacked MCM, the dimensions of the volume element in the $x$ and $y$ directions, as well as the voxel size, are fixed. The contraction is only performed in the stacking direction.
2. In the MCM, all grains are generated during the initialization phase of the algorithm. For the stacked MCM, an initialization phase is performed for each layer. Once a layer is fully generated, the position of the grains of the layer is frozen, and a new layer is initialized on top of the existing one.

Algorithm 2 describes the stacked mechanical contraction method.

We comment on some particular aspects of the algorithm below.

**Remark 1** (*Imposing the Number of Grains or the Layer Thickness?*)**.** In the standard MCM, the number of grains serves as an input parameter. It is also possible to keep it as an input parameter for the stacked MCM. However, the volume of the bunch of grains varies depending on the grains which are sampled (randomly). Therefore, different realizations of the packing algorithm may lead to different volumes of the microstructure. For the stacked MCM, this volume variation leads to a variation of the layer thickness, which is not consistent with the printing procedure. For this reason, we prefer to fix the layer thickness rather than the number of grains. Grains are added to the particle list until the overall volume of grains is greater than the final expected volume of grains $\eta V_{layer}$, where $V_{layer}$ denotes the final volume of the layer and $\eta$ refers to the target volume fraction of grains. Subsequently, the grains are resized so that their total volume matches the expected final volume $V_{grains} = \eta V_{layer}$ exactly. From our experience, the value of the resizing coefficient is always around 0.99 to 1.01, so this re-sizing procedure does not significantly affect the grain size distribution.

**Algorithm 2** Stacked Mechanical Contraction Method

**Inputs**:
Number of layers
Size of each layer
Targeted volume fraction
Minimum distance between the grains
Number of contraction steps

**for** t = 1 to $N_{\text{layers}}$ **do**
  Fix the position of the particles from the previous layers
  **Initialize current layer**:
  Initialize empty particle list
  **while** $V_{grains} < \eta V_{layer}$ **do** ▷ See remark 1
    Sample a cluster of overlapping spheres ▷ See remark 2
  **end while**
  Resize the sampled particles to match exactly the target volume fraction
  Resize the volume element to its initial size
  Sample the initial centroid position $\boldsymbol{c}_i$ and particle orientation $\boldsymbol{R}_i$ of each particle in the initial volume element
  **for** each volume fraction in the list of volume fractions to consider **do**
    **Contraction phase**:
      Resize the volume element
      Move the centroids
    **Overlap removal phase**:
      **while** $\mathcal{E} > 0$ **do**
        Compute overlap energy $\mathcal{E}$ ▷ See remarks 3, 4, 5, eq. (2.7)
        Compute correction
        Translate and rotate particles
      **end while**
  **end for**
**end for**

**Remark 2** (*Particle Sampling*)**.** The particles are chosen from the particle distribution using a scrambled quasi-random sampling (Owen, 2000) based on a Sobol sequence (Sobol, 1967a,b) on the average size of the bounding sphere. Indeed, using a random sampling, the particle statistics would only converge as $N^{-1/2}$ where $N$ stands for the number of particles in the unit cell. A scrambled quasi-random sampling improves this convergence rate up to $N^{-3/2}$ (Owen, 1997). This allows us to keep the unit cell as small as possible while still having a representative grain size distribution inside the unit cell. A study on the representativity of the volume element is presented in Section 3.5.

**Remark 3** (*Reducing the Complexity of the Distance Computation*)**.** When dealing with a large number of spheres, the actual bottleneck is the computation of the distance between all pairs of spheres. To reduce the computational complexity of the overlap checks, the neighbors of each cluster are tracked using Verlet lists (Verlet, 1967), suggested by the initial work of Williams and Philipse (2003) and used by Schneider (2017) for the Sequential Addition and Migration approach. Although this does not reduce the theoretical complexity of the algorithm, the speed-up is significant. Moreover, the computation of the distances can

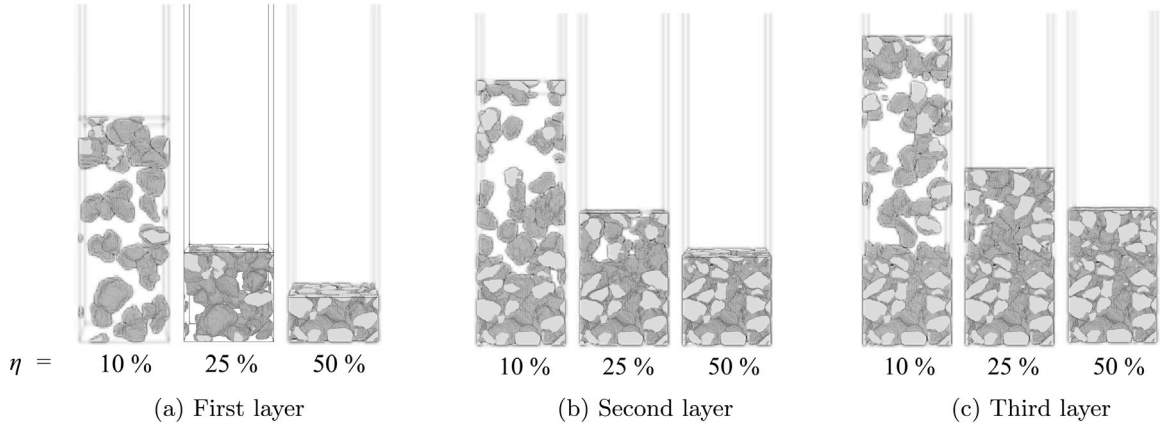


**Fig. 2.** Stacked microstructure generation process for three layers.

be parallelized. Another simple yet powerful trick consists in precomputing the bounding sphere of each cluster of overlapping spheres. The overlap is first checked between the bounding spheres: if the bounding spheres do not intersect, the inscribed grains do not intersect, either. If the bounding spheres intersect, the overlap is only computed for the spheres in the intersection of the bounding spheres.

**Remark 4** (*Periodic and Soft Boundary Conditions*)**.** For homogenization computations, we wish to have periodic microstructures. Indeed, the error on the macroscopic properties is lower if the properties are computed on periodic microstructure compared to non-periodic microstructures (Sab, 1992; Schneider et al., 2022). The periodicity constraint is included in the cluster overlap computation, in all three directions. Furthermore, we impose that the centroid of each particle stays within the layer it was initially generated in. This constraint, which we call "soft boundary constraint", is only enforced in the stacking direction.

**Remark 5** (*Minimum Distance Between Two Particles*)**.** Within the computation of the distance between two particles, a small distance is added, so that two particles are never in contact. This distance avoids continuity between two different particles. Continuity shall only be due to binder bridges. In practice, the generated microstructures are discretized on a regular voxel grid for computations. Hence, the value of the minimum distance is typically chosen equal to the voxel size of the 3D image representing the microstructure.

Fig. 2 shows the stacked mechanical contraction process for three layers with a final volume fraction of 50% in each layer. The indicated volume fraction corresponds to the volume fraction in the layer which is being generated. The volume fraction in the previously generated layers remains at 50%.

### 2.3. Grid-free binder addition

In the 3D printing process, the sand deposit step is followed by the binder addition step. Our microstructure generation approach aims at reproducing the same process. The binder bridges between sand grains arise by capillarity (Erhard et al., 2023; Hartmann et al., 2024). The formation of inter-particle bridges has been, and is still a intense topic of research in physics (Lian et al., 1993; Delenne et al., 2004; Farhat et al., 2024). The capillarity phenomenon was modeled by a closing operation (Serra, 1983) of mathematical morphology previously (Münch and Holzer, 2008; Wang et al., 2018). Such an approach was used in Schneider et al. (2018) and Ettemeyer et al. (2020), as well, to create the desired particle coating. The main drawback of this approach is that the object comprising the clusters of overlapping sphere and the binder does not have a closed-form expression in general, and that the closing operation needs to be evaluated on the grid. Therefore, the actual position of the binder bridges slightly depends on the grid size used for discretization. In this paragraph, we propose to mitigate such drawbacks by a grid-free approach based on the signed distance function and a smooth minimum. A sketch of the steps of the approach is proposed in Fig. 3.

Let us consider a domain $\Omega$ with a boundary $\partial\Omega$. The distance $d$ between a point $\boldsymbol{x}$ and $\partial\Omega$ is defined as:

$$d(\boldsymbol{x}, \partial\Omega) = \inf_{\boldsymbol{y}\in\partial\Omega} d_Y(\boldsymbol{x}, \boldsymbol{y}). \tag{2.9}$$

In the following, the periodic Euclidean distance on the cell $Y$ is considered.

The signed distance function is then defined as follows:

$$f(x) = \begin{cases} -d(\boldsymbol{x}, \partial\Omega) & \text{if } \boldsymbol{x} \in \Omega, \\ d(\boldsymbol{x}, \partial\Omega) & \text{if } \boldsymbol{x} \notin \Omega. \end{cases} \tag{2.10}$$

For a sphere of radius $r$ and of center $\boldsymbol{x}_c$, the signed distance function may be expressed explicitly:

$$f(\boldsymbol{x}) = r - d(\boldsymbol{x}, \boldsymbol{x}_c). \tag{2.11}$$

Fig. 3(a) represents some isovalues of the signed distance function of a sphere occupying the domain $\Omega$.

Interestingly, the outward signed distance function of a union of $N$ objects occupying domains $(\Omega_1, \Omega_2, \dots, \Omega_N)$ can be computed analytically (which is not the case of the inward distance function), as:

$$d(\boldsymbol{x}, \partial(\Omega_1 \cup \Omega_2 \cup \cdots \cup \Omega_n)) = \min_{i=1}^{N} d(\boldsymbol{x}, \partial\Omega_i). \tag{2.12}$$

Hence the outward signed distance function of a union of $N$ spheres of radii $r^i$ and centers $\boldsymbol{x}_c^i$ is:

$$f(\boldsymbol{x}) = \min_{i=1}^{N} \left(r^i - d(\boldsymbol{x}, \boldsymbol{x}_c^i)\right). \tag{2.13}$$

These spheres may belong to different clusters of overlapping spheres, and they may be overlapping or not. Fig. 3(b) shows the outward signed distance function of a cluster of three overlapping spheres occupying the domain $\Omega_1$. Fig. 3(c) shows the outward signed distance function of the union of two clusters, occupying the domains $\Omega_1$ and $\Omega_2$ respectively.

At that point, a smoothing approach can be introduced. Instead of considering a strict minimum, we consider a smooth minimum function (Quilez, 2024). Here we chose to resort to a scaled LogSumExp (LSE) function:

$$\mathrm{LSE}_a(d_1, \dots, d_N) = -a \log\left(\sum_{i=1}^{N} e^{-\frac{d_i}{a}}\right), \tag{2.14}$$

where the scaling parameter $a$ has the dimension of a distance. Its value can be adapted to match the exact volume fraction of binder.

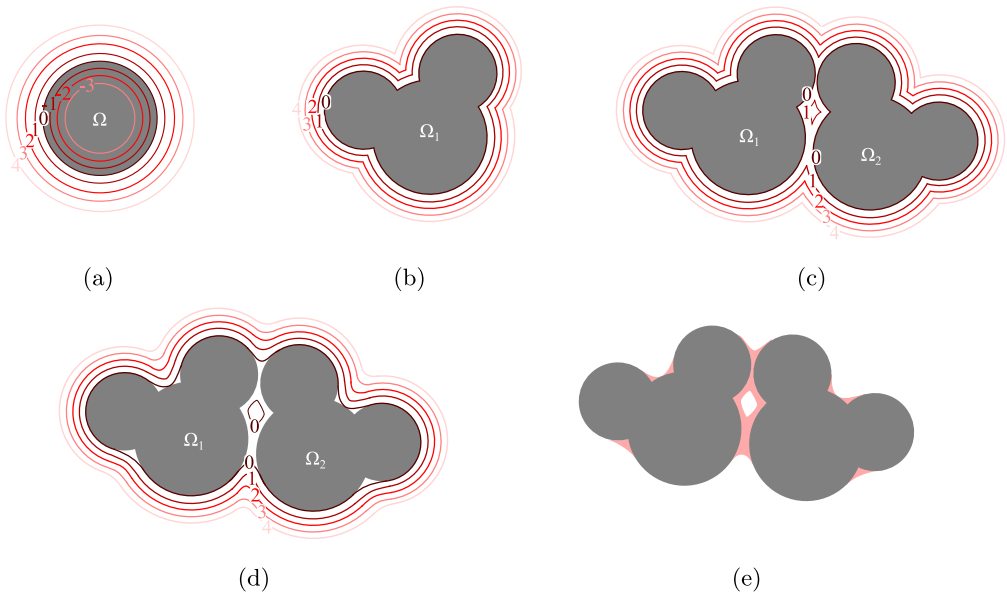


**Fig. 3.** Sketch of the binder addition process.

Then, we define the signed distance of the smoothed union of $N$ spheres as:

$$f_{smooth,a}(\boldsymbol{x}) = \mathrm{LSE}_a(d_1(\boldsymbol{x}), \dots, d_N(\boldsymbol{x})) \tag{2.15}$$

where $d_i$ stands for the value of the signed distance to sphere $i$. In order to speed up the computation, only the $k$th-shortest distances are considered in Eq. (2.15). In the present paper, we consider $k = 5$. The boundary of the smoothed union of spheres $\partial\Omega_{smooth}$ corresponds to the level-set defined by $f_{smooth}(x) = 0$, see Fig. 3(d). Finally, the binder domain, colored in pink in Fig. 3(e), corresponds to the difference between the smoothed union of spheres, defined by $f_{smooth}(x) = 0$, and the initial clusters of spheres, represented in gray. The sand grain domain corresponds to the initial clusters of spheres, in gray in Fig. 3(e). The remaining part of the domain constitutes the pore space. We note that the proposed approach also adds binder between the spheres belonging to the same cluster. This could be avoided by first coating the particles, then performing the binder application process, as it was proposed in Schneider et al. (2018). However, microscopic images show that binder is not only deposited between particles, but also in particle ridges. As adding binder between spheres belonging to the same cluster makes sense from a physical point of view, no specific treatment was applied to remove this binder.

The result of the binder application process is presented in Fig. 4. Fig. 4(a) shows the same microstructure as in Fig. 2 after the addition of a 2 % volume fraction of binder, while Fig. 4(b) presents a slice of the same microstructure. For illustration purpose, Fig. 4(c) shows an electronic microscopy image of a sand-binder composite obtained by 3D printing.

After the discretization process on a voxel grid, the volume fraction of grains and binder may differ from the one targeted. In such a case, the radius of the spheres in the clusters of overlapping spheres and the $a$-coefficient for the binder are slightly adjusted in order to match exactly the target volume fractions in each phase.

## 3. Determination of two macroscopic material properties: elasticity and permeability

### 3.1. Setup for the microstructure generation

The microstructure generation approach described in Section 2 was implemented in Python with Cython extensions. The collision checks between the clusters were parallelized with OpenMP. Unless specified otherwise, the grains are directly sampled from the grains extracted from the $\mu$CT scan mentioned in Section 2.1. First, the grains are sorted based on the diameter of their bounding sphere. Then, the sampling is performed in a quasi-random fashion using a scrambled Sobol sequence (Sobol, 1967a,b), implemented in PyTorch (Paszke et al., 2017). The aim of this procedure is to obtain a grain size distribution in the microstructure that is similar to the one in the initial scan.

The resulting generated volume element occupies the domain:

$$Y = [0, L_x] \times [0, L_y] \times [0, L_z] = [0, \gamma N_x] \times [0, \gamma N_y] \times [0, \gamma N_z], \tag{3.1}$$

where $\gamma$ stands for the resolution of the 3D voxel representation of the microstructure, and $N_x$, $N_y$ and $N_z$ refer to the numbers of voxels in each direction. We consider a subdivision of the domain $Y$ into three non-overlapping subdomains: the subdomain $Y_s$ occupied by the sand grains, the subdomain $Y_b$ occupied by the binder, and the remaining domain $Y_p$ constituting the pore space.

Based on the generated microstructures, we investigate the values of two relevant apparent properties for 3D printed sand cores: the apparent elastic properties and the apparent permeability.

### 3.2. Setup for FFT-based elasticity computations

Regarding the apparent elastic properties, we suppose that the stiffness tensors of the sand phase $\mathbb{C}_s$ and of the binder phase $\mathbb{C}_b$ are given. They define the following stiffness distribution:

$$\mathbb{C}(\boldsymbol{x}) = \begin{cases} \mathbb{C}_s, & \boldsymbol{x} \in Y_s, \\ \mathbb{C}_b, & \boldsymbol{x} \in Y_b, \\ \mathbf{0}, & \text{otherwise.} \end{cases} \tag{3.2}$$

For any given prescribed macroscopic strain $\bar{\boldsymbol{\varepsilon}}$, we seek a displacement field $\boldsymbol{u}_{\bar{\varepsilon}} \in H^1_{\#}(Y)^d$, periodic on the unit cell $Y$, solving the quasistatic balance of linear momentum:

$$\mathrm{div}\, \mathbb{C}(\boldsymbol{x}) : \left(\bar{\boldsymbol{\varepsilon}} + \nabla^s \boldsymbol{u}_{\bar{\varepsilon}}\right) = \mathbf{0}. \tag{3.3}$$

In Eq. (3.3), $\nabla^s$ denotes the symmetrized gradient. The corresponding apparent stress is defined by:

$$\boldsymbol{\sigma}_{\bar{\varepsilon}} = \frac{1}{L_x L_y L_z} \int_Y \mathbb{C}(\boldsymbol{x}) : \left(\bar{\boldsymbol{\varepsilon}} + \nabla^s \boldsymbol{u}_{\bar{\varepsilon}}\right) \mathrm{d}\boldsymbol{x}, \tag{3.4}$$

where $\nabla^s$ refers to the symmetrized gradient and the colon represents a double index contraction. By linearity of the constitutive law, the

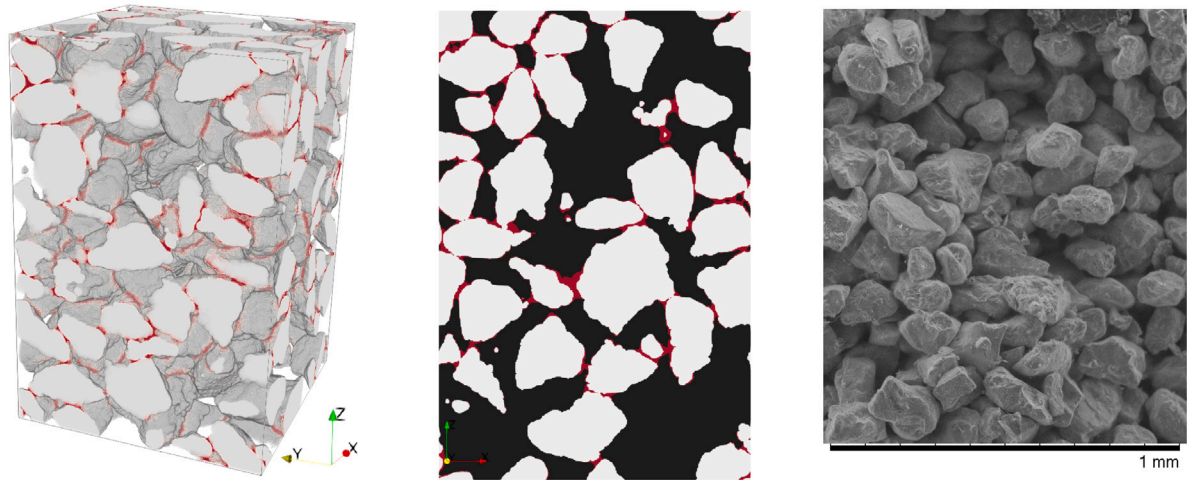


(a) Microstructure generated in figure 2 after the addition of 2 % of red-marked binder

(b) Slice of the microstructure represented in figure 4(a)

(c) Electronic microscopy image of a sand-binder composite

**Fig. 4.** Comparison of the generated microstructure to an electronic microscopy image of the 3D printed material.

dependence of the apparent stress $\boldsymbol{\sigma}_{\bar{\boldsymbol{\varepsilon}}}$ on the imposed strain $\bar{\boldsymbol{\varepsilon}}$ is linear, and may be represented by the apparent stiffness $\mathbb{C}^{\text{app}}$:

$$\boldsymbol{\sigma}_{\bar{\boldsymbol{\varepsilon}}} = \mathbb{C}^{\text{app}} : \bar{\boldsymbol{\varepsilon}}, \tag{3.5}$$

where $\mathbb{C}^{\text{app}}$ is the apparent stiffness.

To fully determine $\mathbb{C}^{\text{app}}$, Eq. (3.3) needs to be solved for six independent load cases, typically chosen as three uniaxial and three shear loadings. We expect the resulting apparent properties to be transversely isotropic in the stacking direction. In order to assess these transversely isotropic properties, the orthotropic engineering constants are computed from $\mathbb{C}^{\text{app}}$ (Cowin, 1985).

Eq. (3.3) is solved by an FFT-based computational micromechanics solver (Moulinec and Suquet, 1994, 1998) implemented in an in-house Python code with Cython extension, using OpenMP for parallelization and the FFTW (Frigo and Johnson, 2005) library to apply the fast Fourier transform. We resort to a conjugate gradient solver (Zeman et al., 2010; Brisard and Dormieux, 2010), and to a staggered grid discretization to ensure stable convergence for porous microstructures (Schneider et al., 2016). Eq. (3.3) is solved to a tolerance $\text{tol} = 10^{-5}$ with regards to the conjugate gradient's convergence criterion presented in Schneider (2021).

In the following, we aim at determining the effective properties of the sand-binder composite, i.e., properties that are statistically representative of the composite (Hill, 1963; Drugan and Willis, 1996). To ensure that the computed apparent stiffness matrix $\mathbb{C}^{\text{app}}$ converges toward the effective stiffness matrix $\mathbb{C}^{\text{eff}}$, the microstructure must occupy a sufficiently large domain $Y$, as defined in Eq. (3.1). In that case, the unit cell $Y$ is called a representative volume element (RVE). A study on the ideal size of the RVE is proposed in Section 3.4.

### 3.3. Setup for permeability computations

To compute the apparent permeability, we follow the same approach as Ettemeyer et al. (2020). For any given mass distributed source density $\boldsymbol{f}$, we seek a periodic velocity field $\boldsymbol{u}_f : Y_\text{p} \to \mathbb{R}^3$ and a periodic pressure field $p_f : Y_\text{p} \to \mathbb{R}$ that comply with the set of equations:

$$\begin{aligned} \mu \Delta \boldsymbol{u}_f + \nabla p_f &= -\boldsymbol{f} \quad \text{in } Y_\text{p}, \\ \operatorname{div} \boldsymbol{u}_f &= \boldsymbol{0} \quad \text{in } Y_\text{p}, \\ \boldsymbol{u}_f &= \boldsymbol{0} \quad \text{on } \partial Y_\text{p}, \end{aligned} \tag{3.6}$$

**Table 1**
Mechanical properties of the sand and the binder.

| | Sand | Binder |
|---|---|---|
| $E$ (GPa) | 66.9 (Daphalapurkar et al., 2011) | 43 (Lechner et al., 2020) |
| $\nu$ | 0.25 (Wichtmann and Triantafyllidis, 2010) | 0.17 (Sanditov et al., 2009) |

where $\mu$ denotes the shear viscosity. Eq. (3.6) encodes the balance of linear momentum, mass conservation and a no-slip boundary condition on the boundary of the pore space $\partial Y_\text{p}$. The velocity field $\boldsymbol{u}_f$ is extended by zero in the solid space $Y \setminus Y_\text{p}$, and its average over the cell $Y$ is:

$$\langle \boldsymbol{u}_f \rangle_Y = \frac{1}{L_x L_y L_z} \int_Y \boldsymbol{u}_f \mathrm{d}\boldsymbol{x} \tag{3.7}$$

Then, the apparent second-order permeability tensor $\boldsymbol{\kappa}^{\text{app}} : Y \to \mathbb{R}^{3\times3}_{\text{sym}}$ is defined as:

$$\langle \boldsymbol{u}_f \rangle_Y = \frac{1}{\mu} \boldsymbol{\kappa}^{\text{app}} . \boldsymbol{f} \tag{3.8}$$

In order to fully determine the permeability tensor $\boldsymbol{\kappa}$, Eq. (3.8) is solved for three independent loading cases, typically $\boldsymbol{f} = \boldsymbol{e}_x$, $\boldsymbol{f} = \boldsymbol{e}_y$ and $\boldsymbol{f} = \boldsymbol{e}_z$.

Because the shear viscosity enters linearly in (3.6) and inversely in (3.8), the effective permeability is independent of the viscosity $\mu$, and depends only on the geometry of the pore space $Y_\text{p}$. The Stokes system (3.6) is discretized by a finite volume method (Wiegmann, 2007) and solved by a LIR solver (Linden et al., 2015) integrated in the software GeoDict (GeoDict, 2023).

### 3.4. Resolution studies

We start by a resolution study concerning the elastic properties of the sand-binder composite and assume that the sand and the binder have an isotropic behavior. We furnish the sand and the binder with the Young's moduli and the Poisson's ratios given in Table 1. They are identical to those chosen in Schneider et al. (2018), except for the binder's Young's modulus which corresponds to the one determined by nanoindentation tests by Lechner et al. (2020) on an inorganic binder. The influence of these local properties on the apparent properties of the sand-binder composite is investigated in more detail in Section 4.2.

First, a resolution study was conducted on a microstructure generated by the aforementioned approach. Such a microstructure is composed of sand grains in a volume fraction of 50 %, bounded by 2 %

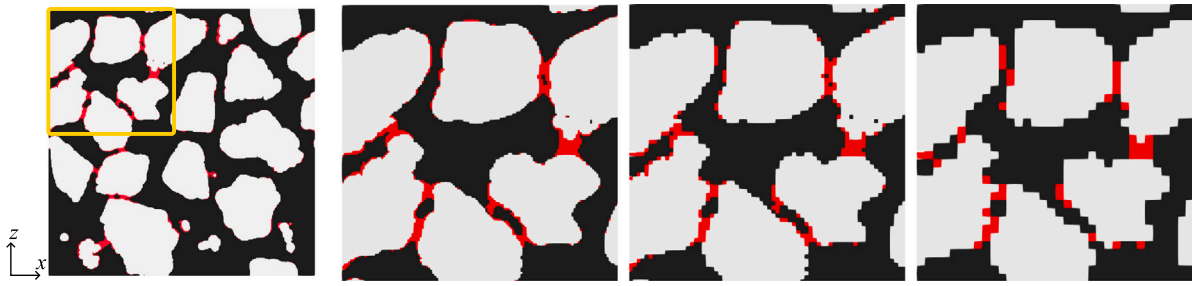


(a) Initial microstructure, zoomed part in yellow (b) Zoom: resolution 2 $\mu$m (c) Zoom: resolution 4 $\mu$m (d) Zoom: resolution 8 $\mu$m

**Fig. 5.** Zoom on a slice of the microstructure for different resolutions. Sand grains are marked in light gray and binder in red.

**Table 2**
Computed apparent orthotropic engineering constants for several resolutions.

| | $E_x$ (GPa) | $E_y$ (GPa) | $E_z$ (GPa) | $G_{yz}$ (GPa) | $G_{zx}$ (GPa) | $G_{xy}$ (GPa) | Relative error to orthotropy (%) |
|---|---|---|---|---|---|---|---|
| 2 µm | 3.10 | 2.96 | 2.83 | 1.20 | 1.27 | 1.38 | 5.3 |
| 4 µm | 3.02 | 2.91 | 2.76 | 1.16 | 1.23 | 1.35 | 6.5 |
| 8 µm | 3.18 | 3.11 | 2.95 | 1.22 | 1.27 | 1.42 | 10.5 |

**Table 3**
Computed apparent permeability for several resolutions.

| | $\kappa_{xx}$ (m$^2$) | $\kappa_{yy}$ (m$^2$) | $\kappa_{zz}$ (m$^2$) | $u_x$ (m s$^{-1}$) | $u_y$ (m s$^{-1}$) | $u_z$ (m s$^{-1}$) |
|---|---|---|---|---|---|---|
| 1 µm | $2.20\times10^{-11}$ | $2.56\times10^{-11}$ | $2.13\times10^{-11}$ | $2.15\times10^{-1}$ | $2.49\times10^{-1}$ | $2.07\times10^{-1}$ |
| 2 µm | $2.23\times10^{-11}$ | $2.59\times10^{-11}$ | $2.14\times10^{-11}$ | $2.17\times10^{-1}$ | $2.51\times10^{-1}$ | $2.09\times10^{-1}$ |
| 4 µm | $2.28\times10^{-11}$ | $2.64\times10^{-11}$ | $2.19\times10^{-11}$ | $2.22\times10^{-1}$ | $2.57\times10^{-1}$ | $2.14\times10^{-1}$ |
| 8 µm | $2.42\times10^{-11}$ | $2.81\times10^{-11}$ | $2.34\times10^{-11}$ | $2.36\times10^{-1}$ | $2.73\times10^{-1}$ | $2.28\times10^{-1}$ |

of inorganic binder. The grains are sampled quasirandomly from the grains extracted from the $\mu$CT scan, based on the diameter of their bounding sphere.

It is composed of two layers of grains, with height 280 µm each. Dimensions in the direction perpendicular to stacking are (560 µm)$^2$. Three different resolutions are considered: 2, 4 and 8 µm per voxel. For this example, a minimal distance of 8 µm, i.e., corresponding to the coarsest resolution, is imposed between the grains. From Fig. 5, representing a part of a slice of the microstructure, it appears that the arrangement of the binder bridges is slightly different with a resolution of 8 µm than for the two finer resolutions.

The computed orthotropic apparent properties are reported in Table 2. The relative error on the moduli computed on the 8 µm-microstructure and on the 2 µm-microstructure is 5.1% at most, while this error is divided by a factor 2 when considering the 4 µm-microstructure and the 2 µm-microstructure. Moreover, the error on the orthotropic approximation decreases from 10.5% to 6.5% when refining the resolution from 8 µm to 4 µm, and to 5.3% when refining it to 2 µm. We conclude that a resolution of 4 µm is refined enough.

We conducted a similar resolution study for the determination of the apparent permeability. As for elasticity, a microstructure composed of sand in a volume fraction of 50 % and binder in a volume fraction of 2 % is considered. The microstructure is composed of two layers of thickness 280 µm, its in-plane size is (560 µm)$^2$, and a minimum distance of 8 µm is imposed between grains. We considered four different resolutions for this parametric study: 1, 2, 4 and 8 µm. Table 3 gathers the results of the resolution study.

Table 3 shows that the apparent permeability and velocities are sensibly higher for a resolution of 8 µm than for the other three resolutions. The results computed with a resolution of 4 µm are around 3 % higher than for a resolution of 1 µm. This gap decreases to around 1 % between the results for a resolution of 2 µm and the results for a resolution of 1 µm. In the following, we resorted to a resolution of 1 µm.

### 3.5. Representativity studies for the apparent elastic properties

For materials with a random microstructure, the apparent properties computed on finite-size microstructure only converge to the effective properties when the size of the cell goes to infinity. Two types of errors are to be expected (Kanit et al., 2003; Gloria and Otto, 2011): a dispersion error on the one hand, and a systematic error, also called bias, on the other hand. The dispersion measures the random fluctuation of properties computed on the microstructures of fixed dimensions (Sab, 1992; Owhadi, 2003), and decreases for increasing cell volume. The bias quantifies the difference between the average properties computed on a fixed-size microstructure and the average properties computed on an infinite size microstructure, and is deterministic (Kanit et al., 2003; Gloria and Otto, 2011). This quantity arises from several factors including correlations induced by the finite size of the cell. Usually, the dispersion and the bias are monitored by increasing all three dimensions of the volume element in the same proportions, see the articles (Schneider et al., 2022; Mehta and Schneider, 2022; Lauff et al., 2024) for instance. In the present case, however, the layer-by-layer generation process influences both the bias and the dispersion. For this reason, we study the effect of the in-plane layer dimension and the effect of the number of layers separately. For both studies, we examine 30 realizations for each cell size, and compute the mean value of the orthotropic engineering constants. The considered material properties are given in Table 1.

First, we consider the in-plane size of the layers. All microstructures feature a resolution of 4 µm, a layer thickness of 280 µm, and their in-plane dimensions range from (280 µm)$^2$ to (1120 µm)$^2$. Fig. 6 shows, in the form of violin plots, the directional elastic moduli for all four microstructure sizes. Each sub-figure corresponds to one direction. In Fig. 6, the average value of each directional modulus is indicated by a white dot.

As it could be expected, the dispersion decreases when the layer size increases. For the (280 µm)$^2$-microstructures, the difference between the lowest and the highest directional modulus in one direction is 3.42 GPa, that is 68% of the mean directional modulus. The latter difference drops to 40% of the mean directional modulus for the (560 µm)$^2$-microstructures, and to 13% for the (560 µm)$^2$-microstructures.

We also note that the average value of the in-plane directional moduli $E_x$ and $E_y$ are similar for the five considered microstructure types. Such results indicate that the bias on the Young's moduli $E_x$ and $E_y$ remains constant for microstructures of in-plane size greater than (280 µm)$^2$. When it comes to the stacking direction, the two smallest microstructures, with the in-plane dimensions (280 µm)$^2$ and (420 µm)$^2$, exhibit a sensible bias on the value of the $E_z$-modulus. Indeed, the mean value of the $E_z$-modulus is 4.3 GPa for the (280 µm)$^2$-microstructures,

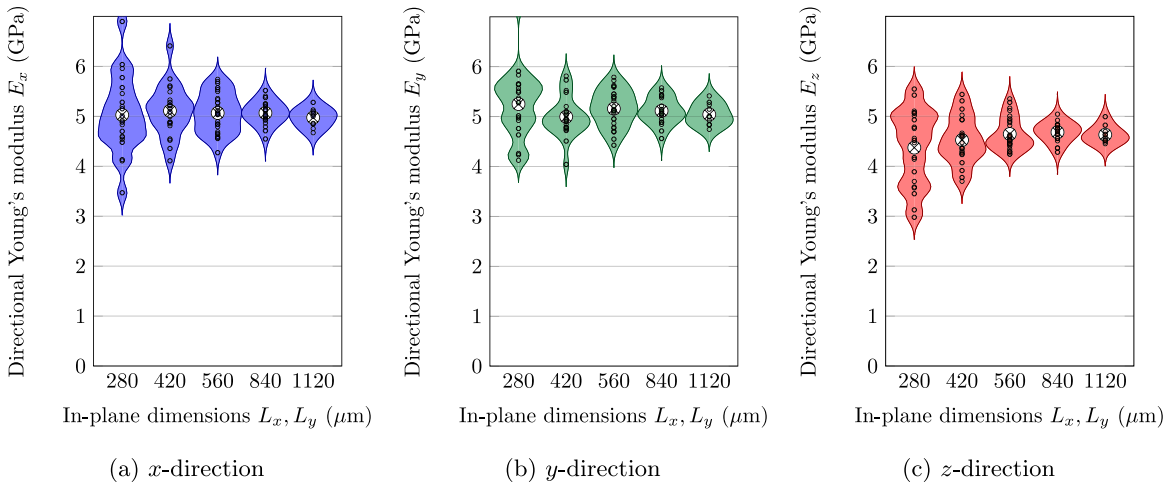


**Fig. 6.** Computed apparent directional moduli for microstructures with two layers and several in-plane dimensions.

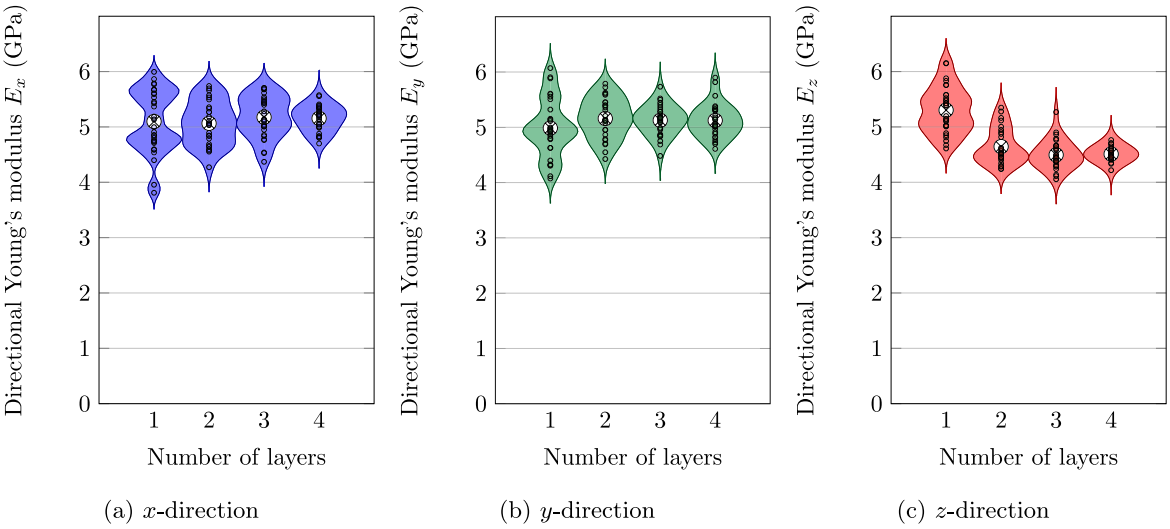


**Fig. 7.** Computed apparent directional moduli for microstructures with several numbers of layers and an in-plane size of (560 μm)$^2$.

and 4.5 GPa for the (420 μm)$^2$-microstructures. It is 8% and 3% less than the value of the $E_z$-modulus on the largest microstructure, respectively. For microstructures with in-plane size of (560 μm)$^2$ and larger, the value of the $E_z$-modulus stabilizes around 4.6 GPa, and does not vary by more than 1% when increasing the size of the microstructure.

We turn our attention to the effect of the number of layers. We generated microstructures with one, two, three and four layers and computed the corresponding macroscopic elastic properties. The in-plane dimensions are fixed to (560 μm)$^2$, the thickness of each layer to 280 μm and the resolution to 4 μm. For each number of layers, 30 different microstructures were generated.

Fig. 7 shows, in the form of violin plots, the directional elastic moduli for all four microstructure types. Each subfigure corresponds to one direction. We note that the dispersion decreases when the number of layer increases. This observation results from an increased number of grains in the microstructure when additional layers are added. Regarding the bias, we observe a major difference between the properties computed on a one-layer-microstructure and the properties computed on microstructures with two layers or more. Indeed, we observe that the properties computed on one-layer microstructures are on average rather close to being isotropic. For two layers and more, the average in-plane elastic moduli $E_x$ and $E_y$ are almost identical, with less than 2 % of difference on the average value. The average out-of-plane elastic modulus $E_z$ is around 0.6 GPa lower, that is around 12 %. Hence, at least two layers are needed in order to generate a transversally isotropic microstructure.

The studies presented in Figs. 6 and 7 confirm the common knowledge that increasing the size of the microstructure often decreases the dispersion (Kanit et al., 2003). However, for larger microstructures, both the microstructure generation time and the computational homogenization time increase. Moreover, if the microstructure comprises a large number of grains, it is more difficult to find a non-overlapping configuration. Sometimes, the microstructure generation process does not converge within the maximal iteration count, fixed at 30 000 iterations here. We study the microstructure generation times for a batch of 30 microstructures, for several layer counts in Fig. 8(a) and Table 4, as well as for several in-plane sizes in Fig. 8(b) and Table 5. The generation times are given for computations conducted on six cores of a workstation featuring a AMD EPYC 9354 processor. In Tables 4 and 5, we also mention the number of tries, i.e., the sum of the successful and unsuccessful generation attempts, needed to generate 30 microstructures.

Concerning the number of layers, we note that the median duration for the generation of the first layer is 235 s. The generation of the second layer then takes much more time: the median generation duration for two layers is 2 126 s. Assuming that the median generation time for the first layer is 235 s, then the median generation time for the second one is 1 891 s. The median generation time for the third

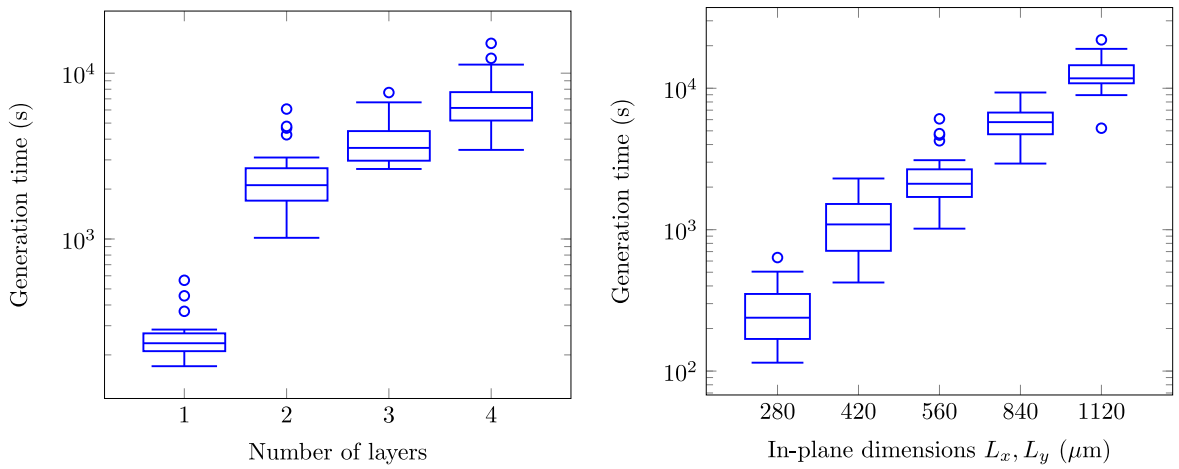


(a) Varying the number of layers for microstructures with a layer size of $(560\ \mu\text{m})^2$

(b) Varying the layer size for microstructures with two layers

**Fig. 8.** Microstructure generation times for different numbers of layers and different layer sizes.

**Table 4**
Statistics on the generation of microstructures with a number of layers ranging from one to four.

| Number of layers | 1 | 2 | 3 | 4 |
|---|---|---|---|---|
| Average generation time (s) | 256 | 2428 | 3983 | 7024 |
| Median generation time (s) | 235 | 2126 | 3566 | 6237 |
| Number of tries | 30 | 33 | 53 | 52 |
| Failure rate (%) | 0 | 9 | 43 | 42 |

**Table 5**
Statistics on the generation of microstructures of several in-plane sizes.

| Layer size ($\mu$m$^2$) | $280^2$ | $420^2$ | $560^2$ | $840^2$ | $1120^2$ |
|---|---|---|---|---|---|
| Average generation time (s) | 256 | 1172 | 2428 | 5970 | 12 697 |
| Median generation time (s) | 246 | 1091 | 2127 | 5934 | 11 969 |
| Number of tries | 40 | 33 | 33 | 59 | 88 |
| Failure rate (%) | 25 | 9 | 9 | 49 | 66 |

layer would then be 1 439 s, and 2 672 s for the fourth one. This difference is due to the presence of fixed grains within the volume for the additional layers. These grains act as boundary conditions and make the process of finding a non-overlapping configuration more complex. This difficulty is also apparent in the number of tries necessary to generate 30 microstructures, presented in Table 4. While all attempts to generate a microstructure were successful for microstructures with one layer, the failure rate increases to 9% to generate microstructures with two layers, and to 42% to generate microstructures with four layers.

When it comes to the size of the layer, Fig. 8(b) shows that increasing the size of the layer leads to a higher generation time. From Table 5, we see that the failure rate surges for microstructures of in-plane size $(1120\ \mu\text{m})^2$. These microstructures comprise more grains, hence the risk of not finding a non-overlapping configuration within 30 000 iterations is higher. What is more surprising is the 25% failure rate for small microstructures with a layer size of $(280\ \mu\text{m})^2$. One possible explanation is that the maximal bounding sphere diameter for the grains is fixed to the layer thickness, that is 280 µm. If a grain with a bounding sphere diameter close to this value is generated, it would fill almost all the space and make a non-overlapping configuration harder to find.

Considering the representativity study presented in Figs. 6 and 7 as well as the generation times presented in Fig. 8, we chose to consider microstructures with an in-plane size of $(560\ \mu\text{m})^2$ and two layers for the rest of the paper. Such layer size and number of layer represent a compromise between a reduced bias and an acceptable generation time.

We turn our attention to the question of the statistical representativity of such microstructures. Let us consider a general unit cell $Y$ comprising the microstructure realization at hand, together with a post-processed scalar quantity of interest $Z(Y)$, e.g., a directional Young's modulus or a directional permeability. As we are concerned with *random* materials, the quantity of interest $Z(Y)$ is a random variable. Under suitable conditions (Kozlov, 1978; Papanicolaou and Varadhan, 1981; Zhikov et al., 1994), the observable $Z(Y)$ converges to an effective quantity $Z^{\text{eff}}$ almost surely in the infinite volume limit

$$Z(Y) \to Z^{\text{eff}} \quad \text{as} \quad \text{vol}(Y) \to \infty. \tag{3.9}$$

Moreover, the effective observable $Z^{\text{eff}}$ turns out to be deterministic. Different authors (Kanit et al., 2003; Gloria and Otto, 2011) noticed the natural decomposition

$$\left\langle |Z(Y) - Z^{\text{eff}}|^2 \right\rangle = |\langle Z(Y)\rangle - Z^{\text{eff}}|^2 + \text{Var}(Z(Y)) \tag{3.10}$$

of the expected deviation, where $\langle\cdot\rangle$ stands for the ensemble average and

$$\text{Var}(Z(Y)) = \left\langle |Z(Y) - \langle Z(Y)\rangle|^2 \right\rangle \tag{3.11}$$

denotes the variance. The first term in Eq. (3.10), called bias or systematic error, is deterministic and measures the inadequacy of the size of the unit cell. By the convergence statement (3.9), the systematic error becomes infinitesimal in the infinite-volume limit. The second summand in Eq. (3.10), called random error or dispersion, measures the variance of the random variable $Z(Y)$.

Suppose that $n > 1$ independent realizations $Z_1(Y), Z_2(Y), \dots, Z_n(Y)$ of the random variable with the same domain $Y$ are given. Then, we may compute the empirical average

$$\frac{1}{n}\sum_{i=1}^{n} Z_i(Y). \tag{3.12}$$

Forming the equivalent of the error decomposition (3.10) yields

$$\left\langle \left| \frac{1}{n}\sum_{i=1}^{n} Z_i(Y) - Z^{\text{eff}} \right|^2 \right\rangle = |\langle Z(Y)\rangle - Z^{\text{eff}}|^2 + \frac{1}{n}\text{Var}(Z(Y)). \tag{3.13}$$

Thus, by drawing a sufficient number of samples on unit cells with a fixed size, the random error may be made as small as possible.

Kanit et al. (2003) introduced an empirical method to estimate the size of a representative volume element. In computational experiments on a number of materials, they made the observation that the systematic error is much smaller than the random error, and converges to zero faster when increasing the unit-cell size. As a consequence, they propose to ignore the systematic error in their considerations. For periodized ensembles, independent studies (Sab and Nedjar, 2005; Schneider et al., 2022) confirm this assumption to be reasonable.

**Table 6**
Statistical analysis of the RVE.

| Property | Exponent | Integral range | In-plane lengths of the RVE $L_x, L_y$ (μm) | | |
|---|---|---|---|---|---|
| | $\alpha$ | $A_3$ (μm$^3$) | $\epsilon_{rel} = 5\%$ | $\epsilon_{rel} = 2.5\%$ | $\epsilon_{rel} = 1\%$ |
| $E_x$ | 1.03 | $26 \times 10^3$ | 1538 | 3011 | 7318 |
| $E_y$ | 0.81 | $2.9 \times 10^3$ | 2215 | 5212 | 16 151 |
| $E_z$ | 1.18 | $71 \times 10^3$ | 1351 | 2431 | 5285 |

Under this assumption, one is left with monitoring the dispersion of the random variable $Z(Y)$. More precisely, the absolute error $\epsilon_{abs}$ and the relative error $\epsilon_{rel}$ of the observable $Z(Y)$ are defined as

$$\epsilon_{abs} = \frac{2}{\sqrt{n}} \sqrt{\mathrm{Var}\,(Z(Y))} \quad \text{and} \quad \epsilon_{rel} = \frac{\epsilon_{abs}}{\langle Z(Y) \rangle}. \tag{3.14}$$

According to Kanit et al. (2003), the cell $Y$ is called a *Representative Volume Element* (RVE) provided the relative error $\epsilon_{rel}$ is lower than the desired value for a single realization, i.e., for $n = 1$.

Based on the works of Lantuejoul (1991) and Kanit et al. (2003) proposed to approximate the variance $\mathrm{Var}\,(Z(Y))$ of the observable by the following power-law relationship:

$$\mathrm{Var}\,(Z(Y)) = D_Z^2 \left( \frac{A_3}{\mathrm{vol}(Y)} \right)^{\alpha}, \tag{3.15}$$

which is assumed to hold at large scales. In Eq. (3.15), $D_Z^2$ refers to the point variance of the quantity $Z$, i.e., the variance of the local Young's moduli if the directional Young's modulus is studied. In Eq. (3.15), the exponent $\alpha$ and the integral range $A_3$ depend on the property investigated. For the considered three-phase material comprising a sand phase, a binder phase and a pore phase, the point variance $D_Z^2$ computes as follows

$$D_Z^2(Y) = \phi_{\mathrm{sand}} E_{\mathrm{sand}}^2 + \phi_{\mathrm{binder}} E_{\mathrm{binder}}^2 - (\phi_{\mathrm{sand}} E_{\mathrm{sand}} + \phi_{\mathrm{binder}} E_{\mathrm{binder}})^2, \tag{3.16}$$

where $\phi_{\mathrm{sand}}$ and $\phi_{\mathrm{binder}}$ stand for the volume fraction of sand and binder, respectively. For a material with sufficiently fast decorrelations, the exponent $\alpha = -1$ is the "natural" one, i.e., the one consistent with the central limit theorem (CLT) scaling in three spatial dimensions.

The values of $\alpha$ and $D_Z^2 {A_3}^{\alpha}$ in Eq. (3.15) may be determined by a linear regression on the logarithmic version of Eq. (3.15), which we performed on the data from Fig. 6 using Scikit-learn (Pedregosa et al., 2011). Table 6 reports on the values of the exponent $\alpha$ and the integral range $A_3$ for the directional Young's moduli $E_x$, $E_y$ and $E_z$.

The values of the variance of the directional moduli $\mathrm{Var}\left(E_i(Y)\right)$ are presented in Fig. 9(a), together with their 90 % confidence interval. From Eqs. (3.14) and (3.15), we may also define the size of the RVE for each property and for a given relative error $\epsilon_{rel}$. These values are also included in Table 6. Please note that we considered volume elements with two layers of 280 μm, and that only the lengths $L_x$ and $L_y$ are varied. Table 6 shows that the expected RVE size is much larger than the size of the microstructures investigated, even for a relative error $\epsilon_{rel} = 5$ %.

Rather than conducting only one computation, we choose to perform $n$ computations on smaller size elements. Fig. 9(b) shows the relationship between the number of independent realizations and the volume of the cell needed to achieve a give relative error $\epsilon_{rel}$. With 30 realizations on a cell of in-plane dimensions $(560\ \mu\mathrm{m})^2$, and comprising two layers of 280 μm, we may expect an error of 2.75% at most on the value of each directional Young's modulus.

To finish with this part, we investigate the symmetries of the apparent stiffness matrix, and more specifically, its distance to an isotropic, a transversely isotropic in the $z$-direction, and an orthotropic stiffness matrix. Table 7 reports on the isotropic, transversely isotropic and orthotropic engineering constant that are computed from the apparent stiffness matrix $\mathbb{C}^{\mathrm{app}}$.

Table 7 shows that, on average, the apparent stiffness matrix of the composite material may be approximated by an orthotropic stiffness matrix with an error of 4.76%, by a transversely isotropic stiffness matrix with an error of 6.66%, and by an isotropic stiffness matrix with an error of 9.48%. To conclude, the apparent elastic properties are on average transversely isotropic in the $z$-direction, but each realization is better described by an orthotropic stiffness matrix than by a transversely isotropic stiffness matrix because of the dispersion of the values. Therefore, in the following, we chose to evaluate the orthotropic stiffness moduli rather than the transversely isotropic ones.

**Table 7**
Average elastic moduli obtained over 30 microstructures.

| | Isotropy | | | |
|---|---|---|---|---|
| Apparent property | $E$ (GPa) | | | Error (%) |
| Average value | 4.81 | | | 9.48 |
| | Transverse isotropy - $z$-direction | | | |
| Apparent property | $E_L$ (GPa) | $E_T$ (GPa) | | Error (%) |
| Average value | 4.63 | 5.07 | | 6.66 |
| | Orthotropy | | | |
| Apparent property | $E_x$ (GPa) | $E_y$ (GPa) | $E_z$ (GPa) | Error (%) |
| Min value | 4.27 | 4.36 | 3.85 | – |
| Average value | 5.07 | 5.11 | 4.63 | 4.76 |
| Max value | 5.74 | 5.79 | 5.35 | – |

## 4. Application and comparison to experiments

### 4.1. A parametric study on the microstructure geometry

The common standard for choosing the layer thickness is to select a thickness between two and three times as large as the median diameter of the grains $D_{50}$, or larger than the largest particle (Mostafaei et al., 2021). Usually, considering a smaller layer thickness leads to a better surface quality, denser samples and high dimensional accuracy (Mostafaei et al., 2021). In contrast, resorting to a large thickness values increases the printing speed (Sivarupan et al., 2021).

Fig. 10 reports on computational investigations on the effect of the layer thickness. Four different layer thicknesses were considered: $1.5D_{50} = 210$ μm, $2D_{50} = 280$ μm, $3D_{50} = 420$ μm and $4D_{50} = 560$ μm. For each value of the layer thickness, 30 different microstructures were generated.

Figs. 10(a) and 10(b) show that the layer thickness has little effect on the in-plane directional moduli $E_x$ and $E_y$. Its effect on the $E_z$-modulus is a bit more sensible, see Fig. 10(c): the average value of $E_z$ increases from 4.45 GPa to 4.77 GPa when the layer thickness increases from 210 μm to 420 μm. We also note that the dispersion of the directional moduli decreases with the layer thickness. This result may come from two different sources. Firstly, an increased layer thickness leads to more grains in the microstructure, and therefore to less dispersion. Secondly, the maximal grain diameter was kept to 280 μm for all experiments. This choice tends to make the packing process more difficult when the layer thickness is lower than 280 μm and to induce more disorder between the grains. However, changing the maximal grain diameter for the different layer thicknesses would have resulted in different grain size distributions. Experimental results showed that increasing the layer thickness reduces the strength (Enneti and Prough, 2019) and the stiffness (Xu et al., 2021) of the sample. We note that the present model does not take into account the binder diffusion within the layer thickness, which is one of the major problems when increasing the layer thickness (Enneti and Prough, 2019) . Hence, we conclude that, when increasing the layer thickness above twice the median diameter $D_{50}$, the observed change in the macroscopic response of the composite are not due to the arrangement of the grains. However, they may come from a heterogeneous distribution of the binder within the layer thickness.

The quality of the parts cast in 3D printed molds is directly related to the binder content of the mold. Molds with high binder content have an increased resistance to erosion and a higher strength (Mitra,

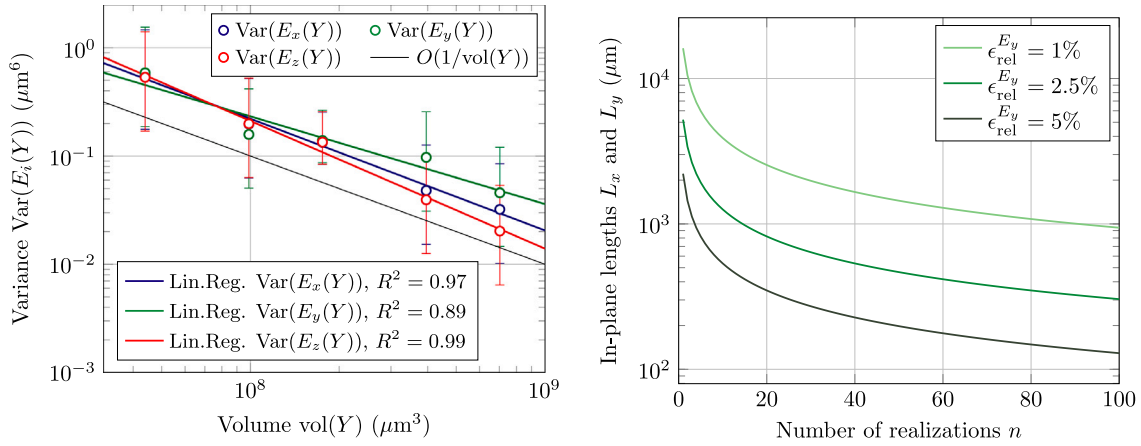


(a) Variance of the directional Young's moduli. The error bars are given for a 90 % confidence interval.

(b) Expected relative error on the $E_y$-modulus

**Fig. 9.** Statistical analysis of the RVE.

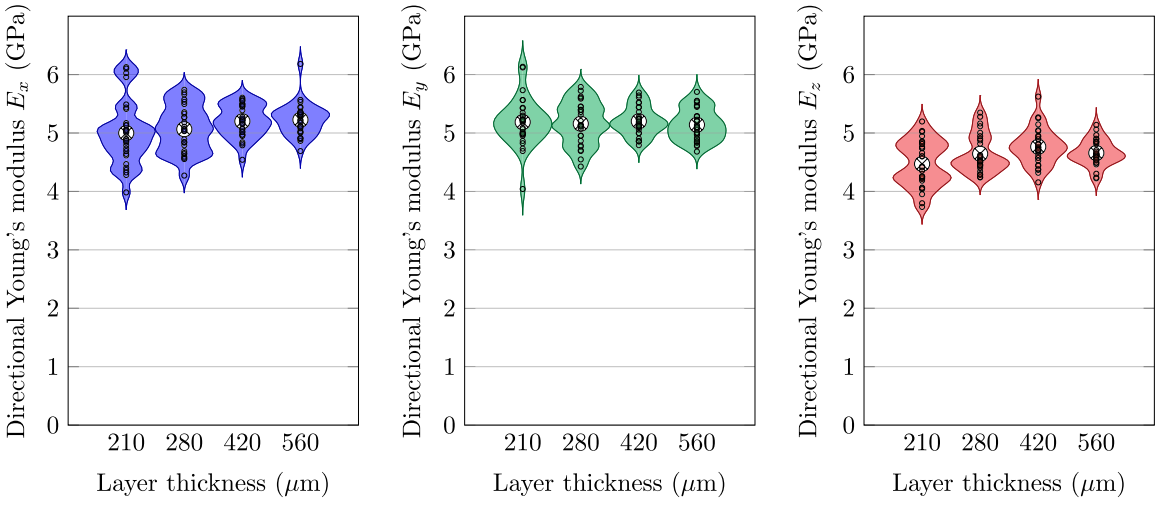


(a) $x$-direction (b) $y$-direction (c) $z$-direction

**Fig. 10.** Distribution of the directional Young's moduli for several layer thicknesses.

2019; Mitra et al., 2019), but too much binder leads to dimensional instabilities (Hodder et al., 2018). Fig. 11 reports the sensitivity of the binder content on the directional Young's moduli. For these investigations, we consider five microstructures composed of two layers of sand grains, with an in-plane dimension of (560 µm)$^2$, extracted from the microstructures generated for the representativity study presented in Table 7. These specific microstructures were chosen because their apparent elastic moduli are close to the average moduli $\bar{E}_i$ ($i = x, y, z$) presented in Table 7. For the parametric study presented in this paragraph, the volume fraction of sand, as well as the position of the grains, stays identical for all volume fractions of binder and for each microstructure.

Figs. 11(a) to 11(c) show that all three directional moduli increase with the binder content. An increase in the binder content also results in a corresponding increase in the difference in the moduli values in all three directions. Such an increase in the differences may result from a bridge pattern formation which is different in the $x$, $y$ and $z$ directions. For illustration purposes, Fig. 11(d) shows some slices of the corresponding microstructures. Please note that these simulation results still need to be confirmed experimentally.

The geometrical percolation ratio of the skeleton, as defined by Kanit et al. (2006), was determined using the MorphoLibJ (Legland et al., 2016) library for Fiji (Schindelin et al., 2012). The percolation ratio is greater than 99.70% for all volume fractions investigated, and for the three directions $x$, $y$ and $z$. Put differently, the skeleton is almost fully connected for a 50 % volume fraction of sand and a volume fraction of binder ranging from 1 to 10 %.

### 4.2. A parametric study on the elastic properties

We turn our attention to the effect of the elastic properties of the sand and binder on the apparent elastic properties of the composite. For these investigations, we consider one microstructure whose apparent properties are close to the average properties presented in Table 7. First, we investigate the effect of the sand's Young's modulus. The latter value is varied between 40 GPa and 115 GPa, while the Young's modulus of the binder and the Poisson's ratio of both materials are kept constant at their values given in Table 1. Fig. 12(a) shows that the directional apparent moduli of the 3D printed composite are linearly dependent on the sand's Young's modulus. The overall apparent stiffness increases with the sand stiffness in the same proportions in all three directions. In particular, the ratios $E_x/E_z$ and $E_y/E_z$ stay almost constant between 1.16 and 1.17 for all values of the sand stiffness. The

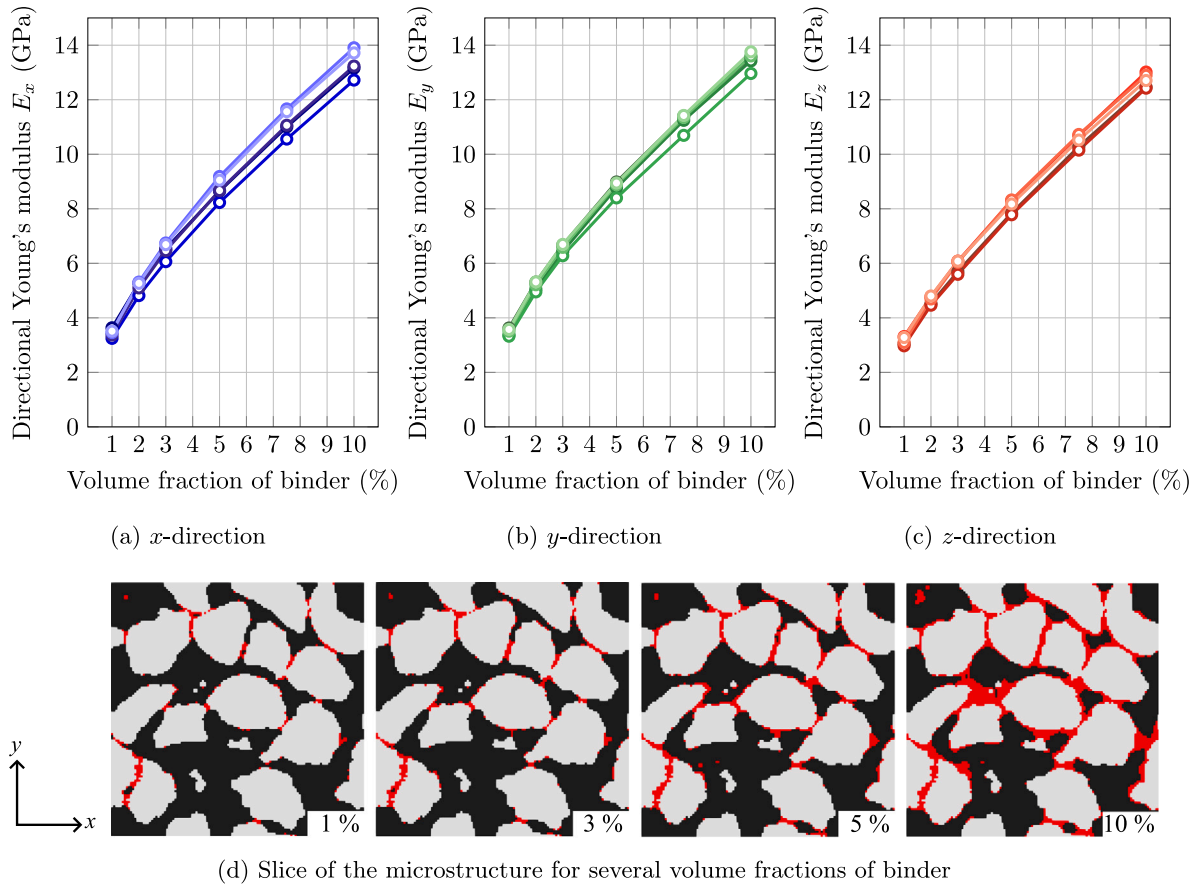


**Fig. 11.** Investigation on the binder content.

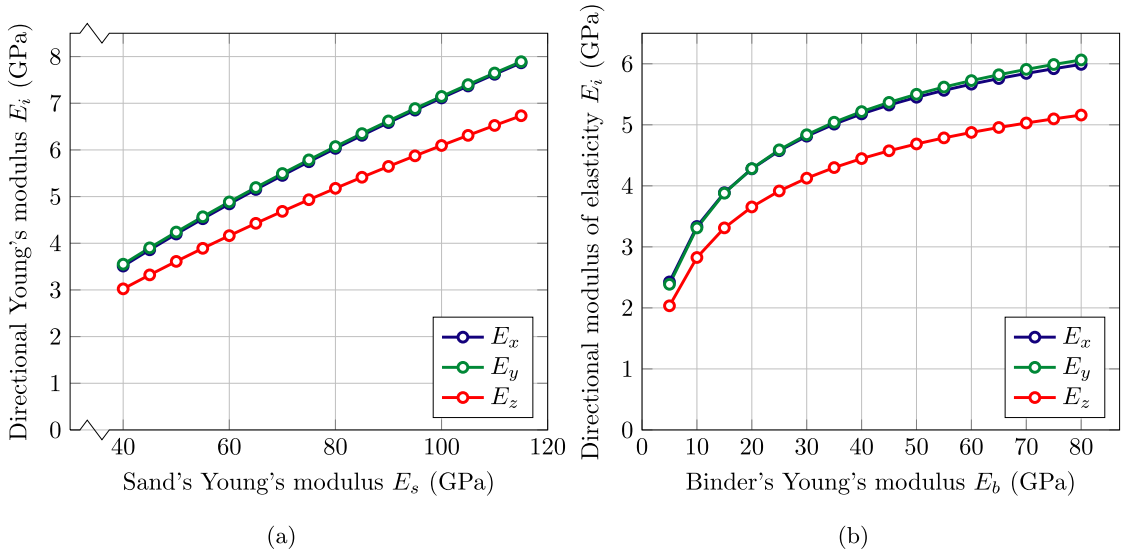


**Fig. 12.** Effect of the variation of the Young's modulus of (a) the sand and (b) the binder on the apparent directional moduli.

linear variation of the moduli is also very similar to the one presented in Schneider et al. (2018) in the context of modeling sand-binder composites obtained by core shooting.

Then, we study the effect of the Young's modulus of the binder on the apparent stiffness of the composite. The Young's modulus value is varied between 5 GPa and 80 GPa. Such a wide range of variation makes the parametric study relevant both for organic binders, whose stiffness can be as low as 5 GPa (Hodder, 2018), and for inorganic binders, whose stiffness can occasionally reach 80 GPa (Lechner et al., 2020). Fig. 12(b) shows that the binder stiffness affects the apparent stiffness in a logarithmic way, rather than in a linear way as for the sand's stiffness. This observation is consistent with the one of Schneider et al. (2018) on shot sand cores. Using a stiff binder reduces the anisotropy very slightly: the $E_x$-modulus is 19 % higher than the $E_z$-modulus when the binder's Young's modulus equal to 5 GPa, while it is only 16 % higher for $E_{binder} = 80$ GPa.

### 4.3. Comparison to experimental results — elasticity

Del Giudice et al. (2024) studied the effect of several parameters including the printing resolution, the binder droplet mass, the printing speed and the binder activator content on the stiffness and strength of a 3D printed sand-binder composite. The samples considered in their study are composed of a GS19-type quartz-sand and of an organic furan binder. Among the different parameters considered, they extract the binder content as a quantity of interest. More specifically, they define the "binder w/v content" as the binder weight per printed bulk material volume ratio.

From the binder w/v content and the density of the binder, it is possible to retrieve an approximation of the binder volume fraction. The density of furfuryl alcohol, the main component of furan, is 1 130 kg m$^{-3}$ (Lide, 2004). We assume that this value coincides with the density of the binder. Under this assumption, the experiments of Del Giudice et al. (2024) cover volume fractions of binder ranging from 2.65% to 4.42%.

We use the microstructure generation approach proposed in the present paper to model the experiments in Del Giudice et al. (2024). The GS19 sand grains are of the same type as the GS14 grains presented in Section 2, however their median diameter $D_{50}$ is 190 μm instead of 140 μm. Therefore, we rescale the clusters of spheres extracted in Section 2.1 by a factor 19/14. We also chose to increase the in-plane size of the microstructure by the same 19/14 factor, leading to an in-plane size of $(760\ \mu m)^2$. The layer thickness is set to 300 μm as indicated by Del Giudice et al. (2024), and each microstructure comprises two layers. The volume fraction of sand is not given. We assumed it to be 50% (Coniglio et al., 2018). We considered three different volume fractions of binder: 2.5%, 3.5% and 4.5%, and generated 30 microstructures for each volume fraction of binder.

For the computations, we used the same sand's Young's modulus and Poisson's ratio as given in Table 1. Obtaining the elastic properties of the binder is more challenging, in particular because the mechanical properties of the binder strongly depend on the curing process (Lechner et al., 2020; Del Giudice and Vassiliou, 2020) and on the additives used. We considered $E_{binder} = 11$ GPa and $\nu_{binder} = 0.17$. The value of the binder Young's modulus was chosen so that the average computed value of the vertical Young's modulus of the printed material $E_z$ is equal to the average experimental value for a volume fraction of binder of 4.5%. Such a value is higher than the ones determined by nanoindentation by Hodder (2018) on a furan binder, between 5.15 GPa and 7.9 GPa depending on the additive. However, Hodder (2018) reports on an experimental Young's modulus of 0.7 to 1.5 GPa for the sand-binder composite. This value is lower than the values presented by Del Giudice et al. (2024) and used in this paragraph.

Fig. 13 reveals a good agreement between the average directional moduli obtained from our model and the ones from Del Giudice et al.'s (2024) experiments. Our microstructure generation approach is able to create microstructures with a degree of anisotropy similar to the one obtained from experiments. It is also able to correctly capture the effect of an increased binder content on the directional Young's moduli of the sand-binder composite. We note that the modeling values feature a larger dispersion than the experimental ones, which may result from the difference in the sample size. Indeed, the experimental samples are around 100 times larger than the numerical volume elements. One possible improvement point for our approach would be to reduce the dispersion without excessively increasing the size of the volume element, and the related computational effort. It would also be of interest to see whether our approach is able to predict the Young's modulus of the sand-binder composite directly from the elastic properties of the sand and the binder.

**Table 8**
Additional information regarding Coniglio et al. (2018)'s experimental study.

| Porosity value | 54% | 51% | 48% |
|---|---|---|---|
| Corresponding volume fraction of sand | 44% | 47% | 50% |
| Corresponding density in kg m$^{-3}$ | 1226 | 1305 | 1383 |

### 4.4. Comparison to experimental results — permeability

Coniglio et al. (2018) studied the effect of the compaction of the sand on the permeability of the mold. The samples they studied are composed of a quartz-sand of median diameter $D_{50} = 140$ μm, printed with a layer thickness of 280 μm. By varying the printing speed, they obtained samples with densities ranging from 1 226 to 1 383 kg m$^{-3}$ and porosity values ranging from 48 to 54 %. Then, the authors tested the permeability of the samples based on an experimental protocol recommended by the American Foundry Society (AFS), described in their paper (Coniglio et al., 2018). This protocol involves measuring the time $t$ required to empty of a chamber of a given volume $Q$, the opening of which is obstructed by a sand core sample of height $h$ and cross-section $S$. The gas permeability $GP$ is then obtained by the following formula:

$$GP = \frac{Q \times h}{S \times p \times t}, \tag{4.1}$$

where $p$ is the pressure expressed in cm Static Pressure Water Gauge (cm SPWG). The time is expressed in minutes, while all dimensions are given in cm. From the expression of the gas permeability $GP$, and assuming an air viscosity of $\mu = 1.8 \times 10^{-5}$ Pa s, we can extract the permeability in its usual S.I. unit m$^2$:

$$\kappa = \mu \times GP \tag{4.2}$$

From a modeling point of view, we consider three porosity values: 48 %, 51 % and 54 %. The corresponding densities, extracted from Coniglio et al. (2018) are given in Table 8. Assuming a volume fraction of binder of 2 %, this leads us to respective volume fractions of sand of 44, 47 and 50 %.

For each of these three cases, we generated 30 microstructures of in-plane dimensions $(560\ \mu m)^2$, comprising two layers of thickness 280 μm, and resolved by 1 μm. In order to outline the benefits of the microstructure generation approach presented in this paper, we add to our investigations microstructures constituted of a polydisperse distribution of spheres and generated using the stacked MCM approach, see Fig. 14(a). The particles' volume distribution is chosen identical for the spheres and for the sand grains. The sphere microstructures feature the same volume fraction of sand and binder, the same number of realizations, the same size and the same resolution as the sand grain microstructures. The average macroscopic permeability values computed on the sand and on the sphere microstructures are gathered in Fig. 14(b).

From Fig. 14(b), we observe that the values of the permeability computed on the sand-based microstructure in the $x$ and $y$ direction are similar, with a 1.5% difference at most between the average values. Still for the sand-based microstructures, the permeability in the $z$-direction is on average 8.7 to 11.5% lower than in the $x$-direction. Such a difference on the average values results from the layer-by-layer microstructure generation process. For illustration, Fig. 15 shows the magnitude of the velocity field for a microstructure with a porosity of 51 %. In Fig. 15(a), the loading is in the $x$-direction, while in Fig. 15(b), it is in the $z$-direction. From these two subfigures, it clearly appears that the flow is slower in the $z$-direction than in the $x$-direction. The permeability values related to the spheres-based microstructures are different from the ones related the sand-based microstructure in two regards. First, the sphere microstructures feature an isotropic flow behavior, on average. Then, the permeability is on average 53% higher for the

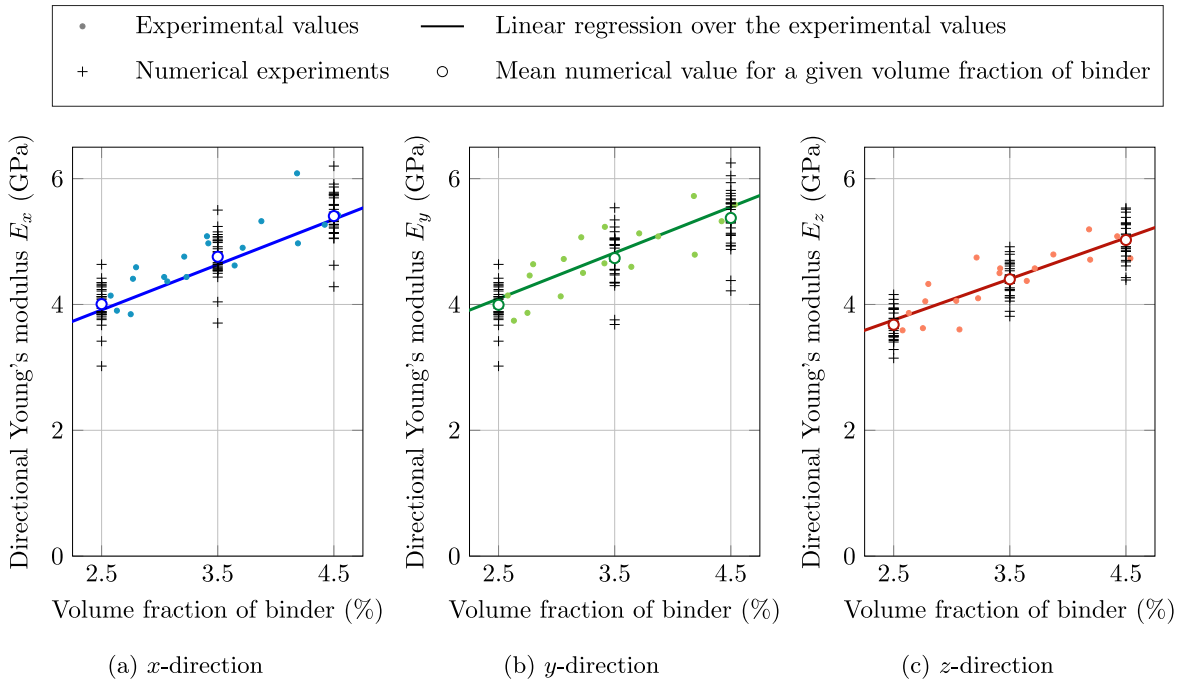


(a) $x$-direction (b) $y$-direction (c) $z$-direction

**Fig. 13.** Comparison between the experimental results presented in Del Giudice et al. (2024) and our numerical results.

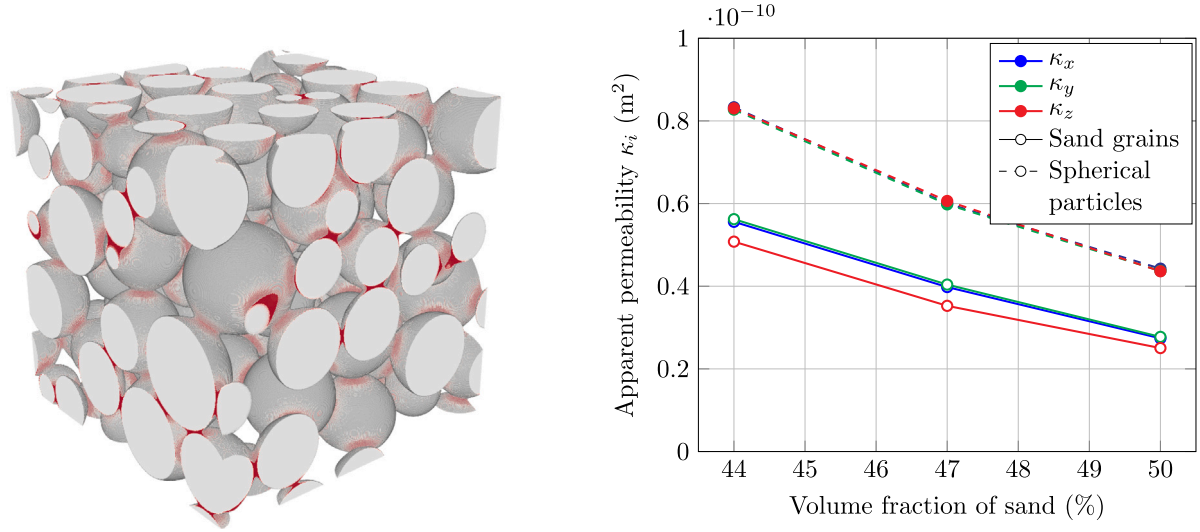


(a) Spheres-based microstructure with a 50 % volume fraction of spheres and 2 % of binder

(b) Average apparent permeability values

**Fig. 14.** Permeability computations on sand-based and spheres-based microstructures.

spheres-based microstructures than for the sand-based microstructure in the $x$ and $y$ directions, and 68% in the $z$-direction.

Fig. 16 compares the experimental results extracted from Coniglio et al. (2018) to the computational results obtained on microstructures composed of sand grains. Focusing first on the computational results, it is interesting to note that the dispersion of the results decreases with the volume of the porous domain. The comparison between the experimental and the computational results shows that the computational results follow the same trend as the experimental ones. The permeability in the $z$-direction is lower than in the $x$-direction. The question of the permeability in the $y$-direction, which is lower than in the $x$-direction in the experiments, was an open question for Coniglio et al. Our model shows similar values of permeability in the $x-$ and $y-$directions. The computations also reproduce the decrease of the permeability when the volume of the porous domain $Y_p$ decreases. However, the experimental permeability values are always slightly lower than the computed ones. This may come from the hypotheses we made on the volume fraction of sand and binder, and the associated density of the sample. To clarify this aspect, it would be interesting to compare the computational results obtained on the generated microstructures to computations on $\mu$CT scans of the microstructure, as it was performed by Ettemeyer et al. (2020). Finally, comparing Figs. 14 and 16 shows that the computation on spheres-based microstructures overestimates the apparent permeability by more than 60 %.

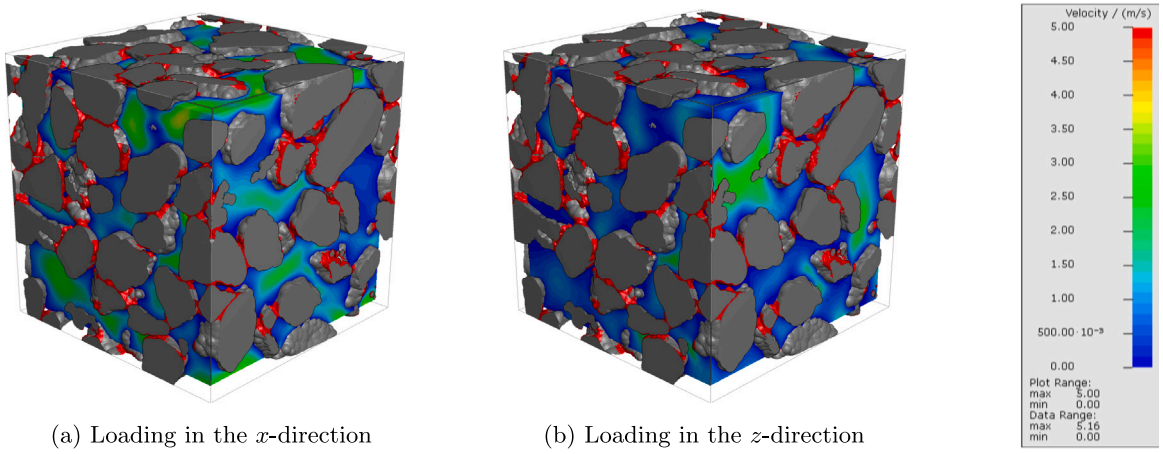


(a) Loading in the $x$-direction (b) Loading in the $z$-direction

**Fig. 15.** Velocity field within the pore space.

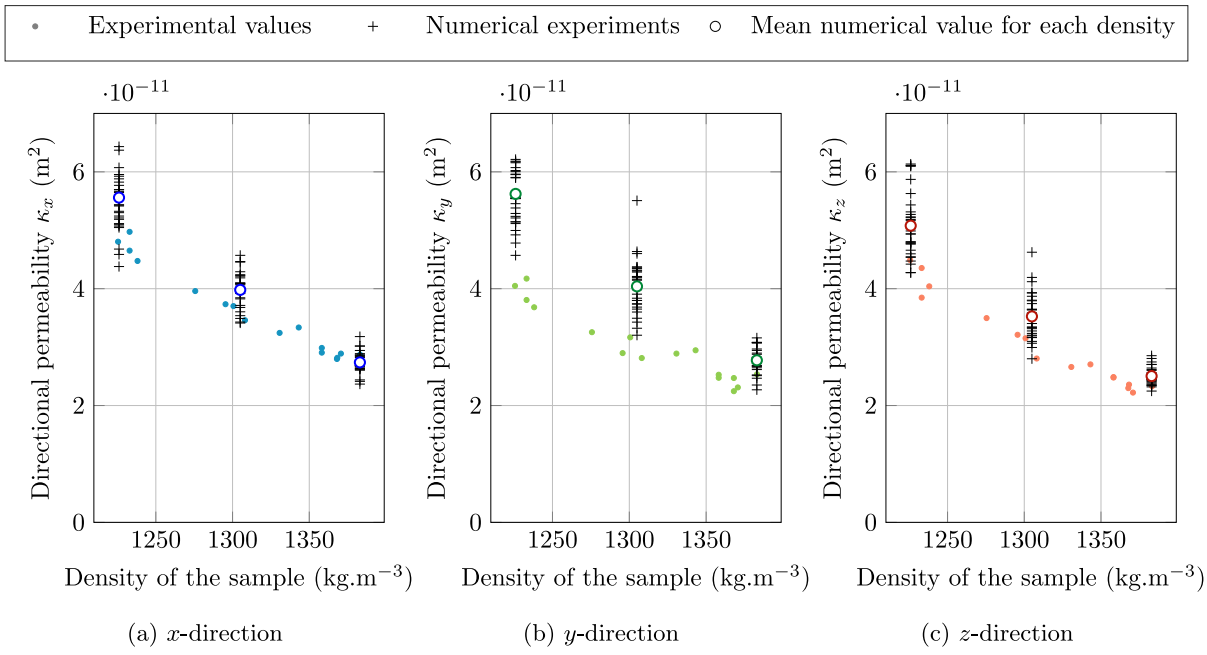


(a) $x$-direction (b) $y$-direction (c) $z$-direction

**Fig. 16.** Comparison between the experimental results presented in Coniglio et al. (2018) and our numerical results.

## 5. Concluding remarks

In the present work, we developed a microstructure generation approach which aims at accounting for the layer-by-layer deposition process of sand based binder-jet 3D-printing. Such an approach relies on a three-step process that features an approximation of CT scans of sand grains images by clusters of overlapping spheres, a stacked mechanical contraction packing approach for the approximated sand grains, and a mesh-free binder addition.

We investigated the necessary size of a volume element and identified a minimum size to avoid bias on the average apparent properties. This study also showed that the introduced microstructure generation approach creates microstructures which are, on average, transversely isotropic in the vertical direction. With regards to the elastic properties, considering a composite material composed of quartz sand and inorganic waterglass binder, the Young's modulus in the vertical direction was around 17 % lower than in the other two directions. The apparent permeability was between 9 and 11 % lower in the vertical direction than in the in-plane directions. While studying the apparent elastic properties, we noted that the dispersion on the values was significant and that it was necessary to compute the apparent properties on at least 30 microstructures for the chosen size of volume element.

Comparison to experimental results showed that our microstructure generation approach accounts for some experimentally observed phenomena, in particular for the transverse isotropy of the printed material. The comparison of our modeling results to the experimental results of Del Giudice et al. (2024) showed excellent agreement between the experimental and numerical values, provided that the binder's Young's modulus is carefully chosen. Comparing the modeled permeability to Coniglio et al.'s (2018) experimental investigations showed that our approach correctly predicts the flow behavior in the $x$ and $z$ directions. The experimental permeability values in the $y$-direction, which are lower than in the $x$-direction, remain unexplained. The computational results were also compared to a simpler approach in which the sand grains were replaced by spheres of identical volume. The latter approach overestimated the apparent permeability by more than 60% and proved unable to predict the anisotropic flow behavior of the microstructure, therefore outlining the relevance of the grain-based microstructure generation approach presented in this paper.

The possible future work concerns both the experimental comprehension of the 3D printing process and its modeling. The different permeability in the two in-plane directions $x$ and $y$ require further experimental investigation, and an adaptation of the current modeling approach. Moreover, a more precise characterization of both the inorganic binder and the sand-binder composite would enable further validation of the modeling approach. In terms of mechanical properties, the sand-binder composite must have a well-defined strength to guarantee that the mold can withstand the thermomechanical stresses induced by the casting process, and breaks easily enough during the decoring phase. Therefore, it would be of interest to develop and experimentally validate a strength homogenization approach. Finally, on the algorithmics side, the microstructure generation algorithm could be improved with respect to the generation time and to the dispersion of the results. In the end, combining the microstructure generation approach presented in this paper to a rigorous experimental validation would permit to determine the relation between the printed geometric microstructure and its thermo-poro-mechanical properties. With such a relation at hand, it would become possible to determine the macroscopic properties of sand cores that comprise other types of sand and binder, as well as to optimize the printing process parameters.

## CRediT authorship contribution statement

**Elodie Donval:** Writing – review & editing, Writing – original draft, Visualization, Validation, Software, Investigation, Formal analysis, Data curation. **Matti Schneider:** Writing – review & editing, Writing – original draft, Supervision, Software, Project administration, Funding acquisition, Conceptualization. **Hannes Grimm-Strele:** Writing – review & editing, Software, Formal analysis. **Michael Godehardt:** Writing – review & editing, Visualization, Data curation. **Raphael Burger:** Writing – review & editing, Investigation, Data curation. **Philipp Lechner:** Writing – review & editing, Visualization, Methodology, Funding acquisition. **Daniel Günther:** Writing – review & editing, Supervision, Funding acquisition. **Heiko Andrä:** Writing – review & editing, Supervision, Funding acquisition.

## Declaration of competing interest

The authors declare that they have no known competing financial interests or personal relationships that could have appeared to influence the work reported in this paper.

## Acknowledgments

Funding by the Deutsche Forschungsgemeinschaft (DFG, German Research Foundation) – 507778349 – is gratefully acknowledged by all the authors. MS acknowledges support from the European Research Council within the Horizon Europe program - project 101040238. We thank Franz Schreiber, Benjamin Bauer and Katja Schladitz (Department of Image Processing, Fraunhofer ITWM Kaiserslautern) for the $\mu$CT-scans and the particles segmentation, and the anonymous reviewers for their constructive comments.

## Data availability

Data will be made available on request.

## References

Alshembar, A., Kronenberger, M., Burgmann, S., Schladitz, K., Breit, W., 2024. Separation of sand and gravel particles in volume images using a random forest. Materials Today Communications (ISSN: 2352-4928) 41, 110957.

Andrä, H., Combaret, N., Dvorkin, J., Glatt, E., Han, J., Kabel, M., Keehm, Y., Krzikalla, F., Lee, M., Madonna, C., Marsh, M., Mukerji, T., Saenger, E.H., Sain, R., Saxena, N., Ricker, S., Wiegmann, A., Zhan, X., 2013a. Digital rock physics benchmarks—Part I: Imaging and segmentation. Comput. Geosci. 50, 25–32.

Andrä, H., Combaret, N., Dvorkin, J., Glatt, E., Han, J., Kabel, M., Keehm, Y., Krzikalla, F., Lee, M., Madonna, C., Marsh, M., Mukerji, T., Saenger, E.H., Sain, R., Saxena, N., Ricker, S., Wiegmann, A., Zhan, X., 2013b. Digital rock physics benchmarks—Part II: Computing effective properties. Comput. Geosci. 50, 33–43.

Andrade, J.E., Lim, K.-W., Avila, C.F., Vlahinić, I., 2012. Granular element method for computational particle mechanics. Comput. Methods Appl. Mech. Engrg. 241, 262–274.

Angelidakis, V., Nadimi, S., Otsubo, M., Utili, S., 2021. CLUMP: a code library to generate universal multi-sphere particles. SoftwareX 15, 100735.

Bargmann, S., Klusemann, B., Markmann, J., Schnabel, J.E., Schneider, K., Soyarslan, C., Wilmers, J., 2018. Generation of 3D representative volume elements for heterogeneous materials: A review. Prog. Mater. Sci. 96, 322–384.

Bennett, C.H., 1972. Serially deposited amorphous aggregates of hard spheres. J. Appl. Phys. 43 (6), 2727–2734.

Beucher, S., 1994. Digital skeletons in Euclidean and geodesic spaces. Signal Process. 38 (1), 127–141.

Blum, H., 1967. A transformation for extracting new descriptions of shape. Model. Percept. Speech Vis. Form 362–380.

Borgefors, G., 1984. Distance transformations in arbitrary dimensions. Comput. Vis. Graph. Image Process. 27, 321–345.

Braun, P., Tzortzopoulos, G., Stefanou, I., 2021. Design of sand-based, 3-D-printed analog faults with controlled frictional properties. J. Geophys. Res.: Solid Earth 126 (5), e2020JB020520.

Brisard, S., Dormieux, L., 2010. FFT-based methods for the mechanics of composites: A general variational framework. Comput. Mater. Sci. 49 (3), 663–671.

Burgmann, S., Godehardt, M., Schladitz, K., Breit, W., 2022. Separation of sand and gravel particles in 3D images using the adaptive h-extrema transform. Powder Technol. 404, 117468.

Coniglio, N., Sivarupan, T., El Mansori, M., 2018. Investigation of process parameter effect on anisotropic properties of 3D printed sand molds. Int. J. Adv. Manuf. Technol. 94, 2175–2185.

Cowin, S.C., 1985. The relationship between the elasticity tensor and the fabric tensor. Mech. Mater. 4 (2), 137–147.

Cundall, P.A., Strack, O.D.L., 1979. A discrete numerical model for granular assemblies. Géotechnique 29 (1), 47–65.

Dana, H.R., El Mansori, M., 2020. Mechanical characterisation of anisotropic silica sand/furan resin compound induced by binder jet 3D additive manufacturing technology. Ceram. Int. 46 (11), 17867–17880.

Danielsson, P.E., 1980. Euclidean distance mapping. Comput. Graph. Image Process. 14 (3), 227–248.

Daphalapurkar, N.P., Wang, F., Fu, B., Lu, H., Komanduri, R., 2011. Determination of mechanical properties of sand grains by nanoindentation. Exp. Mech. 51, 719–728.

DeJong, M.J., Vibert, C., 2012. Seismic response of stone masonry spires: Computational and experimental modeling. Eng. Struct. 40, 566–574.

Del Giudice, L., Marelli, D., Sudret, B., Vassiliou, M.F., 2024. Global sensitivity analysis of 3D printed material with binder jet technology by using surrogate modeling and polynomial chaos expansion. Prog. Addit. Manuf. 9 (2), 375–389.

Del Giudice, L., Vassiliou, M.F., 2020. Mechanical properties of 3D printed material with binder jet technology and potential applications of additive manufacturing in seismic testing of structures. Addit. Manuf. 36, 101714.

Delenne, J.-Y., El Youssoufi, M.S., Cherblanc, F., Bénet, J.-C., 2004. Mechanical behaviour and failure of cohesive granular materials. Int. J. Numer. Anal. Methods Geomech. 28 (15), 1577–1594.

Delloro, F., Jeandin, M., Jeulin, D., Proudhon, H., Faessel, M., Bianchi, L., Meillot, E., Helfen, L., 2017. A morphological approach to the modeling of the cold spray process. J. Therm. Spray Technol. 26, 1838–1850.

Drugan, W.J., Willis, J.R., 1996. A micromechanics-based nonlocal constitutive equation and estimates of representative volume element size for elastic composites. J. Mech. Phys. Solids 44 (4), 497–524.

Dvorkin, J., Berryman, J., Nur, A., 1999. Elastic moduli of cemented sphere packs. Mech. Mater. 31 (7), 461–469.

Dvorkin, J., Nur, A., Yin, H., 1994. Effective properties of cemented granular materials. Mech. Mater. 18 (4), 351–366.

Enneti, R.K., Prough, K.C., 2019. Effect of binder saturation and powder layer thickness on the green strength of the binder jet 3D printing (BJ3DP) WC-12% Co powders. Int. J. Refract. Met. Hard Mater. 84, 104991.

Erhard, P., Tanjavooru, V.T., Hartmann, C., van den Bosch, L., Seidel, A., Volk, W., Günther, D., 2023. Simulation of binder infiltration in additive manufacturing of sand molds. Adv. Eng. Mater. 25 (20), 2300212.

Ettemeyer, F., Lechner, P., Hofmann, T., Andrä, H., Schneider, M., Grund, D., Volk, W., Günther, D., 2020. Digital Sand Core Physics: Predicting physical properties of sand cores by simulations on digital microstructures. Int. J. Solids Struct. 188–189, 155–168.

Farhat, A., Luu, L.-H., Doghmane, A., Cuéllar, P., Benahmed, N., Wichtmann, T., Philippe, P., 2024. Micro and macro mechanical characterization of artificial cemented granular materials. Granul. Matter 26 (3), 65.

Feder, J., 1980. Random sequential adsorption. J. Theoret. Biol. 87 (2), 237–254.

Ferellec, J.-F., McDowell, G.R., 2010. A method to model realistic particle shape and inertia in DEM. Granul. Matter 12, 459–467.

Frigo, M., Johnson, S.G., 2005. The design and implementation of FFTW3. In: Proceedings of the IEEE. Vol. 93, pp. 216–231.

Garcia, X., 2009. Numerical Modelling of the Microstructure and Permeability of Granular Materials (Ph.D. thesis). Imperial College London.

Garcia, X., Latham, J.-P., Xiang, J., Harrison., J., 2009. A clustered overlapping sphere algorithm to represent real particles in discrete element modelling. Géotechnique 59 (9), 779–784.

2023. GeoDict Simulation Software. Math2Market GmbH, Kaiserslautern, Germany, http://www.geodict.de. Release 2023.

Gloria, A., Otto, F., 2011. An optimal variance estimate in stochastic homogenization of discrete elliptic equations. Ann. Probab. 39 (3), 779–856.

Hartmann, C., Silberhorn, J., Erhard, P., Günther, D., 2024. On the mechanism of binder migration in furan binder jetting of sand molds and cores. Addit. Manuf. 83, 104073.

Hill, R., 1963. Elastic properties of reinforced solids: some theoretical principles. J. Mech. Phys. Solids 11 (5), 357–372.

Hodder, K.J., 2018. Fabrication, Characterization and Performance of 3D-Printed Sandstone Models (Ph.D. thesis). University of Alberta.

Hodder, K.J., Nychka, J.A., Chalaturnyk, R.J., 2018. Process limitations of 3D printing model rock. Prog. Addit. Manuf. 3, 173–182.

Hosseininia, E.S., Mirghasemi, A.A., 2006. Numerical simulation of breakage of two-dimensional polygon-shaped particles using discrete element method. Powder Technol. 166 (2), 100–112.

Kanit, T., Forest, S., Galliet, I., Mounoury, V., Jeulin, D., 2003. Determination of the size of the representative volume element for random composites: statistical and numerical approach. Int. J. Solids Struct. 40 (13–14), 3647–3679.

Kanit, T., N'Guyen, F., Forest, S., Jeulin, D., Reed, M., Singleton, S., 2006. Apparent and effective physical properties of heterogeneous materials: Representativity of samples of two materials from food industry. Comput. Methods Appl. Mech. Engrg. 195 (33–36), 3960–3982.

Katagiri, J., Matsushima, T., Yamada, Y., 2010. Simple shear simulation of 3D irregularly-shaped particles by image-based DEM. Granul. Matter 12, 491–497.

Kong, L., Ostadhassan, M., Hou, X., Mann, M., Li, C., 2019. Microstructure characteristics and fractal analysis of 3D-printed sandstone using micro-CT and SEM-EDS. J. Pet. Sci. Eng. 175, 1039–1048.

Kozlov, S.M., 1978. Averaging of differential operators with almost periodic rapidly oscillating coefficients. Math. USSR-Sb. 107 (149) (2 (10)), 199–217.

Lantuejoul, C., 1991. Ergodicity and integral range. J. Microsc. 161 (3), 387–403.

Lauff, C., Schneider, M., Montesano, J., Böhlke, T., 2024. Generating microstructures of long fiber reinforced composites by the fused sequential addition and migration method. Internat. J. Numer. Methods Engrg. 125 (22), e7573.

Lechner, P., Filippov, P., Kraschienski, N., Ettemeyer, F., Volk, W., 2020. A novel method for measuring elastic modulus of foundry silicate binders. Int. J. Met. 14, 423–431.

Legland, D., Arganda-Carreras, I., Andrey, P., 2016. MorphoLibJ: integrated library and plugins for mathematical morphology with ImageJ. Bioinformatics 32 (22), 3532–3534.

Li, C.-Q., Xu, W.-J., Meng, Q.-S., 2015. Multi-sphere approximation of real particles for DEM simulation based on a modified greedy heuristic algorithm. Powder Technol. 286, 478–487.

Lian, G., Thornton, C., Adams, M.J., 1993. A theoretical study of the liquid bridge forces between two rigid spherical bodies. J. Colloid Interface Sci. 161 (1), 138–147.

Lide, D.R., 2004. CRC Handbook of Chemistry and Physics, vol. 85, CRC Press.

Lienhard, J., Barisin, T., Grimm-Strele, H., Kabel, M., Schladitz, K., Schweiger, T., 2024. Microstructural characterisation of 3D printed and injection-moulded glass fibre-reinforced polypropylene by image analysis, simulation and experimental methods. Strain 60 (2), e12463.

Linden, S., Wiegmann, A., Hagen, H., 2015. The LIR space partitioning system applied to the Stokes equations. Graph. Model. 82 (C), 58–66.

Lu, Y., Tan, Y., Li, X., Liu, C., 2017. Methodology for simulation of irregularly shaped gravel grains and its application to DEM modeling. J. Comput. Civ. Eng. 31 (5), 04017023.

Lu, G., Third, J.R., Müller, C.R., 2015. Discrete element models for non-spherical particle systems: From theoretical developments to applications. Chem. Eng. Sci. 127, 425–465.

Lubachevsky, B.D., Stillinger, F.H., 1990. Geometric properties of random disk packings. J. Stat. Phys. 60, 561–583.

Mavko, G., Mukerji, T., Dvorkin, J., 2020. The Rock Physics Handbook. Cambridge University Press.

Mehta, A., Schneider, M., 2022. A sequential addition and migration method for generating microstructures of short fibers with prescribed length distribution. Comput. Mech. 70 (4), 829–851.

Mitra, S., 2019. Experimental and Numerical Characterization of Functional Properties of Sand Molds Produced by Additive Manufacturing (3D Printing by Jet Binding) in a Fast Foundry (Ph.D. thesis). Ecole nationale supérieure d'Arts et Métiers-ENSAM.

Mitra, S., de Castro, A.R., El Mansori, M., 2019. On the rapid manufacturing process of functional 3D printed sand molds. J. Manuf. Process. 42, 202–212.

Mitra, S., El Mansori, M., de Castro, A.R., Costin, M., 2020. Study of the evolution of transport properties induced by additive processing sand mold using X-ray computed tomography. J. Mater. Process. Technol. 277, 116495.

Mitra, S., Rodríguez de Castro, A., El Mansori, M., 2018. The effect of ageing process on three-point bending strength and permeability of 3D printed sand molds. Int. J. Adv. Manuf. Technol. 97, 1241–1251.

Mostafaei, A., Elliott, A.M., Barnes, J.E., Li, F., Tan, W., Cramer, C.L., Nandwana, P., Chmielus, M., 2021. Binder jet 3D printing—Process parameters, materials, properties, modeling, and challenges. Prog. Mater. Sci. 119, 100707.

Moulinec, H., Suquet, P., 1994. A fast numerical method for computing the linear and nonlinear mechanical properties of composites. C. R. Acad. Sci. Sér. II Mécanique Phys. Chim. Sci. Univers Sci. Terre 318 (11), 1417–1423.

Moulinec, H., Suquet, P., 1998. A numerical method for computing the overall response of nonlinear composites with complex microstructure. Comput. Methods Appl. Mech. Engrg. 157, 69–94.

Münch, B., Holzer, L., 2008. Contradicting geometrical concepts in pore size analysis attained with electron microscopy and mercury intrusion. J. Am. Ceram. Soc. 91 (12), 4059–4067.

Osher, S., Sethian, J.A., 1988. Fronts propagating with curvature-dependent speed: Algorithms based on Hamilton-Jacobi formulations. J. Comput. Phys. 79 (1), 12–49.

Owen, A.B., 1997. Scrambled net variance for integrals of smooth functions. Ann. Statist. 25 (4), 1541–1562.

Owen, A.B., 2000. Monte Carlo, quasi-Monte Carlo, and randomized quasi-Monte Carlo. In: Monte-Carlo and Quasi-Monte Carlo Methods 1998: Proceedings of a Conference Held at the Claremont Graduate University, Claremont, California, USA, June 22–26, 1998. Springer, pp. 86–97.

Owhadi, H., 2003. Approximation of the effective conductivity of ergodic media by periodization. Probab. Theory Related Fields 125, 225–258.

Papanicolaou, G.C., Varadhan, S.R.S., 1981. Boundary value problems with rapidly oscillating random coefficients. In: Random Fields, Vol. I, II (Esztergom, 1979). In: Colloq. Math. Soc. János Bolyai, vol. 27, North-Holland, Amsterdam-New York, pp. 835–873.

Paszke, A., Gross, S., Chintala, S., Chanan, G., Yang, E., DeVito, Z., Lin, Z., Desmaison, A., Antiga, L., Lerer, A., 2017. Automatic differentiation in PyTorch. In: NIPS Autodiff Workshop.

Pedregosa, F., Varoquaux, G., Gramfort, A., Michel, V., Thirion, B., Grisel, O., Blondel, M., Prettenhofer, P., Weiss, R., Dubourg, V., Vanderplas, J., Passos, A., Cournapeau, D., Brucher, M., Perrot, M., Duchesnay, E., 2011. Scikit-learn: Machine learning in Python. J. Mach. Learn. Res. 12, 2825–2830.

Pilotti, M., 1998. Generation of realistic porous media by grains sedimentation. Transp. Porous Media 33, 257–278.

Preece, D.S., Jensen, R.P., Perkins, E.D., Williams, J.R., 1999. Sand production modeling using superquadric discrete elements and coupling of fluid flow and particle motion. In: ARMA US Rock Mechanics/Geomechanics Symposium. ARMA, pp. ARMA–99.

Quilez, I., 2024. Smooth minimum. https://iquilezles.org/articles/smin/. (Accessed 17 October 2024).

Sab, K., 1992. On the homogenization and the simulation of random materials. Eur. J. Mech. A Solids 11, 585–607.

Sab, K., Nedjar, B., 2005. Periodization of random media and representative volume element size for linear composites. C. R. Mécanique 333 (2), 187–195.

Sanditov, D.S., Mantatov, V.V., Sanditov, B.D., 2009. Poisson ratio and plasticity of glasses. Tech. Phys. 54 (4), 594–596.

Sattari, A.S., Rizvi, Z.H., Motra, H.B., Wuttke, F., 2017. Meso-scale modeling of heat transport in a heterogeneous cemented geomaterial by lattice element method. Granul. Matter 19, 1–12.

Schindelin, J., Arganda-Carreras, I., Frise, E., Kaynig, V., Longair, M., Pietzsch, T., Preibisch, S., Rueden, C., Saalfeld, S., Schmid, B., et al., 2012. Fiji: an open-source platform for biological-image analysis. Nature Methods 9 (7), 676–682.

Schneider, M., 2017. The Sequential Addition and Migration method to generate representative volume elements for the homogenization of short fiber reinforced plastics. Comput. Mech. 59, 247–263.

Schneider, M., 2021. A review of non-linear FFT-based computational homogenization methods. Acta Mech. 232, 2051–2100.

Schneider, M., Hofmann, T., Andrä, H., Lechner, P., Ettemeyer, F., Volk, W., Steeb, H., 2018. Modeling the microstructure and computing effective elastic properties of sand core materials. Int. J. Solids Struct. 143, 1–17.

Schneider, M., Josien, M., Otto, F., 2022. Representative volume elements for matrix-inclusion composites - a computational study on the effects of an improper treatment of particles intersecting the boundary and the benefits of periodizing the ensemble. J. Mech. Phys. Solids 158, 104652.

Schneider, M., Ospald, F., Kabel, M., 2016. Computational homogenization of elasticity on a staggered grid. Internat. J. Numer. Methods Engrg. 105 (9), 693–720.

Serra, J., 1983. Image Analysis and Mathematical Morphology. Academic Press, Inc.
Seshadri, B., Ravi, K.S.D., Hischier, I., Schlueter, A., 2021. Investigating mechanical and thermo-physical properties of binder jet 3D printed elements using a statistical experiment approach. Rapid Prototyp. J. 27 (9), 1709–1730.
Sethian, J.A., 1999. Fast marching methods. SIAM Rev. 41 (2), 199–235.
Shen, Z., Huang, D., Wang, G., Zhao, Y., Jin, F., 2022. A mesoscale bond model for discrete element modeling of irregular cemented granular materials. Comput. Geotech. 152, 105051.
Sivarupan, T., Balasubramani, N., Saxena, P., Nagarajan, D., El Mansori, M., Salonitis, K., Jolly, M., Dargusch, M.S., 2021. A review on the progress and challenges of binder jet 3D printing of sand moulds for advanced casting. Addit. Manuf. 40, 101889.
Sivarupan, T., El Mansori, M., Daly, K., Mavrogordato, M.N., Pierron, F., 2019. Characterisation of 3D printed sand moulds using micro-focus X-ray computed tomography. Rapid Prototyp. J. 25 (2), 404–416.
Sobol, I.M., 1967a. On the distribution of points in a cube and the approximate evaluation of integrals. USSR Comput. Math. Math. Phys. 7 (4), 86–112.
Sobol, I.M., 1967b. Uniformly distributed sequences with additional uniformity properties. USSR Comput. Math. Math. Phys. 16, 236–242.
Soltanbeigi, B., Podlozhnyuk, A., Papanicolopulos, S.-A., Kloss, C., Pirker, S., Ooi, J.Y., 2018. DEM study of mechanical characteristics of multi-spherical and superquadric particles at micro and macro scales. Powder Technol. 329, 288–303.
Sonon, B., François, B., Massart, T.J., 2012. A unified level set based methodology for fast generation of complex microstructural multi-phase RVEs. Comput. Methods Appl. Mech. Engrg. 223, 103–122.
Theocharis, A., Roux, J.-N., Langlois, V., 2020. Elasticity of model weakly cemented granular materials: A numerical study. Int. J. Solids Struct. 193, 13–27.
Topin, V., Delenne, J.-Y., Radjaı, F., Brendel, L., Mabille, F., 2007. Strength and failure of cemented granular matter. Eur. Phys. J. E 23, 413–429.
Torquato, S., Jiao, Y., 2010. Robust algorithm to generate a diverse class of dense disordered and ordered sphere packings via linear programming. Phys. Rev. E 82 (6), 061302.
Upadhyay, M., Sivarupan, T., El Mansori, M., 2017. 3D printing for rapid sand casting—A review. J. Manuf. Process. 29, 211–220.
Verlet, L., 1967. Computer "experiments" on classical fluids. I. Thermodynamical properties of Lennard-Jones molecules. Phys. Rev. 159 (1), 98.
Wang, H., Jeulin, D., Willot, F., Sorbier, L., Moreaud, M., 2018. Modelling of the microstructure of mesoporous alumina constrained by morphological simulation of nitrogen porosimetry. Colloids Surf. A: Physicochem. Eng. Asp. 553, 378–396.
Weissbach, R., Praegla, P.M., Wall, W.A., Hart, A.J., Meier, C., 2024. Exploration of improved, roller-based spreading strategies for cohesive powders in additive manufacturing via coupled DEM-FEM simulations. Powder Technol. 119956.
Wichtmann, T., Triantafyllidis, T., 2010. On the influence of the grain size distribution curve on P-wave velocity, constrained elastic modulus $M_{max}$ and Poisson's ratio of quartz sands. Soil Dyn. Earthq. Eng. 30 (8), 757–766.
Wiegmann, A., 2007. Computation of the permeability of porous materials from their microstructure by FFF-Stokes. Berichte Fraunhofer ITWM 127.
Williams, J.W.J., 1964. Algorithm 232 - Heapsort. Commun. ACM 7 (6), 347–349.
Williams, S., Philipse, A., 2003. Random packings of spheres and spherocylinders simulated by mechanical contraction. Phys. Rev. E—Stat. Nonlinear Soft Matter Phys. 67, 1–9.
Xu, Q., Jiang, L., Ma, C., Niu, Q., Wang, X., 2021. Effect of layer thickness on the physical and mechanical properties of sand powder 3D printing specimens. Front. Earth Sci. 9, 763202.
Yuan, F.-L., 2019. Combined 3D thinning and greedy algorithm to approximate realistic particles with corrected mechanical properties. Granul. Matter 21 (2), 19.
Zeman, J., Vondřejc, J., Novak, J., Marek, I., 2010. Accelerating a FFT-based solver for numerical homogenization of periodic media by conjugate gradients. J. Comput. Phys. 229 (21), 8065–8071.
Zhang, J., Tan, Y., Xiao, X., Jiang, S., 2022. Comparison of roller-spreading and blade-spreading processes in powder-bed additive manufacturing by DEM simulations. Particuology 66, 48–58.
Zhang, K., Zhang, K., Ye, J., Liu, X., Fan, W., 2023. An improved sand 3D printing method for better reproduction of high-strength and high-brittleness rock mechanical properties is proposed. J. Mater. Res. Technol. 26, 5037–5054.
Zhao, Y., Jiang, L., Li, C., Niu, Q., Sainoki, A., Mitri, H.S., Ning, J., 2023. Experimental investigation into the mechanical behavior of jointed soft rock using sand powder 3D printing. Rock Mech. Rock Eng. 56 (7), 5383–5404.
Zhikov, V.V., Kozlov, S.M., Oleinik, O.A., 1994. Homogenization of Differential Operators and Integral Functionals. Springer-Verlag, New York.
Zhou, T., Zhu, J.B., 2018. Identification of a suitable 3D printing material for mimicking brittle and hard rocks and its brittleness enhancements. Rock Mech. Rock Eng. 51, 765–777.